

AD-A092 781

RENSSELAER POLYTECHNIC INST TROY N Y
THE INFLUENCE OF COHERENCY STRAIN ON THE ELEVATED TEMPERATURE T-ETC(U)
DEC 80 D A GROSE, G S ANSELL
N00014-76-C-0458

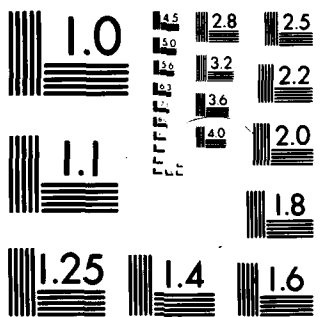
NL

UNCLASSIFIED

TR-11

1-1
AD-A092 781

END
DATE FILMED
1-81
DTIC



MICROCOPY RESOLUTION TEST CHART
NATIONAL BUREAU OF STANDARDS

AD A092781

LEVEL ✓

(2) ^{4W}

(1) Technical Report No. 11

to

(14) TR-11

OFFICE OF NAVAL RESEARCH

Contract N00014-76-C-0458 NR 031-689/12-9-77(471)

Entitled

(6) THE INFLUENCE OF COHERENCY STRAIN ON THE ELEVATED TEMPERATURE
TENSILE BEHAVIOR OF Ni-15Cr-Al-Ti-Mo Alloys.

Submitted by

(10) D. A. Grose ■ G. S. Ansell
Rensselaer Polytechnic Institute
Troy, New York 12181



Submitted for publication to
The Metallurgical Transactions

(11) December 1980

(12) 74

Reproduction in whole or in part is permitted for any purpose of the
United States Government. Distribution of this document is unlimited.

302100

LB

80 12 10 052

DDC FILE COPY

THE INFLUENCE OF COHERENCY STRAIN ON THE ELEVATED TEMPERATURE TENSILE BEHAVIOR OF Ni-15Cr-Al-Ti-Mo ALLOYS

D. A. Grose
IBM Data Systems Division, East Fishkill
Hopewell Junction, New York 12533

G. S. Ansell
Rensselaer Polytechnic Institute
Troy, New York 12180

ABSTRACT

The effect of coherency strain on elevated temperature tensile strength was examined in a model, two-phase γ -strengthened Ni-15Cr-Al-Ti-Mo alloy series. The temperature dependence of coherency strain as represented by the $\gamma-\gamma'$ mismatch was determined over the temperature range 25°C to 300°C. The flow stress increment $\Delta\sigma_{\gamma'}$, due to precipitation of γ' , was found to correlate well to the magnitude of the $\gamma-\gamma'$ mismatch over the same temperature interval. The correlation was strongest for high misfit alloys regardless of the Antiphase Boundary Energy (APBE). The predominance of by-pass type dislocation-particle interactions in high coherency alloys confirms that strengthening is primarily due to coherency strains. Conversely, alloys with low misfit exhibit two distinct particle shear mechanisms believed to be dependent upon the relative APBE and matrix stacking fault energy of the alloy.

Accession For				
NTIS GRA&I	<input type="checkbox"/>	<input type="checkbox"/>	<input type="checkbox"/>	
DTIC T&B				
Unannounced				
Justification				
By _____	Distribution/	Availability Codes	Avail and/or	Distri
			Special	A

INTRODUCTION

The most significant contribution to the strength of nickel-base alloys results from the coherent precipitation of γ' , the intermetallic phase, which has a stoichiometry based on $\text{Ni}_3\text{Al}(\text{Ti})$. This phase possesses an order Ll_2 type structure, and has been shown to remain fully ordered up to a temperature very near its melting point.¹ Several studies on a variety of precipitation-hardenable alloy systems have presented unequivocal experimental evidence supporting coherency strain strengthening as a major determinant of low temperature mechanical behavior. Nevertheless, the importance of coherency strain as an elevated temperature particle-strengthening mechanism in γ' , precipitating nickel-base alloys, remains inexplicit.

Nordheim and Grant² contributed early evidence that coherency strengthening in γ' -bearing Ni-Cr-Al-Ti alloys brought about significant increases in hardness and stress-rupture properties. The work of Mihalisin and Decker³ on Ni-Al-Ti binary and ternary alloys showed that maximum age hardness in both room temperature and hot hardness tests was obtained at a Ti/Al atomic ratio of approximately 1.7. Optimum age hardening was directly correlated to the disregistry between the lattices of the γ and γ' phases, and the resultant coherency strains. A subsequent detailed study by Mihalisin and Decker⁴ was made to provide a critical test of the hypothesis that substitution of elements for Al in γ' of Ni-Al alloys could alter the hardness by changing the coherency strains. Judicious selection of ternary additions provided a range of γ - γ' misfits, while the effects of APBE and solid solution hardening were monitored. They concluded that age

hardening could be enhanced by alloying, which increased mismatch and coherency strains. Decker and Mihalisin pointed out that under conditions of non-diffusional creep ($T < 0.5T_m$), coherency strains may benefit strengthening, whereas low coherency strains are desired for $T > 0.6T_m$ in order to minimize $\gamma-\gamma'$ surface energy, and thus maximize phase stability.

Mirkin and Kancheev⁵ investigated the relationship of creep properties to differences in lattice spacing (Δa) between the γ' and γ phases in a series of Ni-Cr-Al alloys. They established that longer creep lives and minimum steady-state creep rates correlate to the minimum value of Δa . Maniar and Bridge⁶ provided a critical test for the postulate that γ' mismatch and resultant coherency strains have a significant influence on stress-rupture properties of a nickel-base alloy. They found, in agreement with Mirkin and Kancheev, that a lower $\gamma-\gamma'$ mismatch was beneficial to stress-rupture life.

In contrast to the findings of Mirkin-Kancheev and Maniar-Bridge, a few investigators have found large misfits to enhance creep resistance. Nordheim and Grant reported that substitution of Ti atoms for Al in the $Ni_3(Al,Ti)$ lattice increased the misfit between the γ and γ' phases, and raised the creep-rupture strength of Ni-Cr-Ti-Al alloys. Pfeil et al.⁷ showed the elevated temperature strength of a series of Nimonic 80-type alloys was also related to the effect of variation in the Ti and Al contents. The highest creep resistance was observed when the Ti/Al ratio of the alloys fell between 5 and 13. The influence of increased Ti/Al ratio on mismatch and its effect on improving creep resistance may

be fortuitous since the Ti/Al ratio of γ' , in addition to varying the γ - γ' mismatch, has a concomitant effect on the APBE of γ' .⁸⁻¹² Therefore, as a result of these investigations, the relationship of large coherency strains to elevated temperature behavior is unclear.

The contribution of coherency strengthening was effectively demonstrated in the nickel-base Alloy 713 by Oblak et al.¹³ As predicted by coherency strengthening models, the temperature dependence of the critical resolved shear stress was shown to follow that of the modulus despite the high estimated APBE of the γ'' (Ni_3Nb) phase.

Munjal and Ardell¹⁴ demonstrated that the contribution of coherency hardening in an underaged Ni-12.19 atomic percent (at.%) Al alloy is roughly equivalent in magnitude to that due to order strengthening, and is very strongly temperature dependent. The values of the increment in critical resolved shear strength were found, nevertheless, to be temperature independent, leading Munjal and Ardell to conclude that the contribution of coherency strengthening was negligible. A subsequent study by Ardell, et al.,¹⁵ on Ni-Al single crystals with larger volume fractions of γ' , found those conventional theories of order strengthening unable to predict the magnitude of strengthening in higher volume fraction alloys. Ardell noted that in view of the similar temperature dependencies of the flow stress and lattice mismatch, the contribution of coherency strains in alloys aged to peak strength may be significant.

Goodrum and Lefevre¹⁶ studied the strength characteristics and microstructure as a function of aging time and temperature in aged Ni-Mo alloys containing ordered, coherent precipitates. The observed negative dependence of the flow stress on temperature was attributed to coherency strain strengthening.

Miller and Ansell investigated the room temperature mechanical behavior in the same Ni-Cr-Al-Ti-Mo alloy series used in our study. The fraction of γ' precipitate was found to be the major factor in influencing flow strength in these nickel-base alloys. In addition, they demonstrated that a linear correlation existed between the measured γ - γ' mismatch and the strength of these alloys after accounting for variations in the weight fraction of γ' .

The study of coherent particle-strengthened systems and the applicability of coherency strengthening models have been confined mainly to low temperature mechanical behavior in nickel-base alloys. The present investigation examines the role of coherency strain on elevated temperature tensile behavior in a model series of γ' -precipitating nickel alloys based on the Ni-Cr-Al-Ti-Mo system. Since the temperature dependence of coherency strains is unpredictable from low temperature measurements, we determined the temperature dependence of the γ - γ' misfit. Elevated temperature tensile tests were performed on single phase, non-precipitation hardenable alloys to provide an estimate of the properties of the γ' strengthened alloys in the solutionized condition. Mechanical property-structure relationships were established using transmission electron microscopy in order to interpret and

substantiate the influence of coherency strain on elevated temperature alloy behavior.

MATERIALS

In this investigation, we used a series of alloys based upon the Ni-Cr-Al-Ti-Mo system originally designed by Miller and Ansell for the study of the significant strengthening factors in nickel-base, γ' -precipitating alloys. This alloy system is well characterized,^{8,17,18} and is ideal for the study of coherency strengthening, since large variations in the γ - γ' misfit with minimum changes in the chemistry and volume fraction of γ' formed are possible.

Systematic variations in alloying additions were made within this model Ni-Cr-Al-Ti-Mo alloy series in order to separate the effects of coherency strain, antiphase boundary energy (APBE), and weight fraction of γ' . The use of alloy additions to influence the magnitude of either the γ or γ' lattice constant may produce variations in coherency strain. Coherency strain, as represented by the unconstrained γ - γ' lattice mismatch, δ , is given by:

$$\delta = \frac{a_o^{\gamma'} - a_o^\gamma}{a_o^\gamma}$$

where:

$a_o^{\gamma'}$ = lattice constant of γ' measured when separated from the bulk alloy, and

a_o^γ = lattice constant of the matrix phase.

Aluminum and titanium have been shown to partition preferentially to γ' ,¹⁹ and therefore influence the γ - γ' mismatch. The Ti/Al

ratio of γ' , in addition to having a strong effect on the γ - γ' mismatch,^{17,19} has been connected to the APBE of γ' .⁸⁻¹² Significant variations in the coherency strain may be generated using these additions; however the chemistry of the γ' , and hence the APBE is altered.

Chromium and molybdenum partition mainly to the γ matrix phase,^{19,20} altering the phase's lattice constant and the resulting γ - γ' mismatch. Molybdenum provides a large expansion of the γ lattice parameter and exhibits relatively large solubilities in nickel and its alloys. Loomis¹⁷ has concluded that Mo has virtually no effect on the Al and Ti contents of γ' , and that substitution of Ti for Al significantly reduces the solubility of Mo and Cr in γ' . Thus, Mo additions provide a convenient means of altering the γ - γ' mismatch without influencing the chemistry of the γ' and APBE.

Results drawn from the initial Miller-Ansell investigation of this Ni-15Cr-Al-Ti-Mo system allow the structuring of four groups of alloys based upon general coherency strain and APBE properties (see Table I). A fifth group acts as controls to determine the extent of solid solution strengthening. Groups A and B separate the high and low APBE alloys that exhibit high coherency strain. Although the coherency strain of alloy number 8 is relatively high, the APBE, which is significantly influenced by the Ti/Al ratio,⁸⁻¹² should be lower than Group A alloys. A single alloy may only partially represent the behavior of a high coherency, low APBE alloy group; nevertheless the properties of alloy 8 are varied enough from those of Group A to warrant this separate group.

Groups C and D distinguish between alloys with different APBE at low coherency strain. The Ti/Al ratio of Group C alloys is 1.8 and suggests that a relatively high APBE exists for alloys in this group. The APBE of alloy number 10 has been measured to be 0.2 Jm^{-2} .⁸ Conversely, Group D represents low APBE alloys at low coherency strain. The Ti/Al ratio for each alloy in Group D is zero; the APBE of alloy number 11 is 0.133 Jm^{-2} .⁸

Group E alloy numbers 16, 17, and 18 are controls that measure the extent of solid solution strengthening. Alloy 16 was designed to determine the effect of Mo on solid solution strengthening; alloy 17, the potent effect of Al; and alloy 18, the combined influence of Al and Ti. Each control alloy is non-precipitation hardenable and permits making an estimate of the properties of alloys, in the absence of γ' .

Table II lists the actual composition, in atomic percent, of the experimental alloy series. Small amounts of boron and carbon were added to all alloys to improve the hot working characteristics and to stabilize the grain size. Alloys 4 through 7, 15, 17, and 18 were prepared by Allegheny Ludlum Steel Corporation, Brackenridge, Pa. Electrolytic grade elemental materials, with the exception of boron, which was added as NiB, were used as starting materials.

The remaining alloys were prepared by Special Metals Corporation, New Hartford, N.Y. The International Nickel Company, Suffern, N.Y. performed the extrusion. Again, with the exception of boron, which was added as NiB, starting materials for these alloy heats also consisted of high purity elemental materials.

EXPERIMENTAL PROCEDURE

Precision Lattice Parameter Measurements

We used X-ray diffraction to measure the precise lattice parameters for the γ matrix and γ' precipitate phases, thus allowing us to determine the γ - γ' mismatch over the temperature interval 25°C to 300°C. To facilitate the collection of extracted γ' and to minimize X-ray line broadening due to particle size effects, all measurements were made on specimens aged for 1000 hours at 760°C. Loomis, et al.¹⁷ have shown on alloys with similar compositions to those used in this study, that the average change in $a_0^{\gamma'}$ is less than 0.01 nm between aging times of 63 and 1000 hours at 760°C. In addition, Miller²¹ noted that $a_0^{\gamma'}$ changes significantly on initial aging, and is followed by a small shift between the 1 hour and 1000 hour values.

We made matrix lattice parameter measurements on bulk specimens; whereas γ' lattice constants were determined on powder samples obtained by electrolytic phase extraction²² of the γ' phase from appropriately heat treated bulk samples.

We used an X-ray diffractometer/high temperature vacuum stage technique employing a 99.999% gold powder standard to minimize systematic errors and to provide a reference between samples.^{21,23} Thermal expansion data for 99.999% gold came from the work of Simmons and Balluffi.²⁴ The lattice constant for gold, determined for each test temperature, was based on the 25°C value, $a_0 = 0.407855$ nm, taken from Pearson's compilation.²⁵

The high temperature vacuum stage had two chromel-alumel thermocouple probes. The signal from one thermocouple acted as a sensor for a digital power supply. The second thermocouple was imbedded in the specimen for temperature measurement. With this arrangement, we obtained temperature variations of $\pm 2^\circ\text{C}$ at 800°C .

Values of the X-ray diffraction angle, 2θ , for the alloy {220} reflection of Cr K_α radiation were used to calculate a_0^γ and $a_0^{\gamma'}$. In addition, at a number of test temperatures, we made several replicate measurements of alloy lattice parameters using the {331} reflection of Cu K_α radiation.

Tensile Testing

We performed tensile tests on control alloys 16, 17, and 18 over the temperature range 25°C to 800°C . The temperature dependence of the flow stress of these non-precipitation hardenable alloys provides an estimate of the effect of solid solution strengthening. All machined specimens for tensile testing were first solution-heat-treated at 1150°C for two hours in an inert atmosphere, and then drop-quenched into -30°C iced brine.

We did tensile testing on an Instron testing machine outfitted for elevated temperature testing with a furnace and stainless steel test chamber. Specimen temperature was controlled to within $\pm 5^\circ\text{C}$, and all tests were performed in an inert atmosphere. Specimen elongation was measured using an Instron

2.54-cm, 10 percent longitudinal strain gage extensometer mounted below the furnace. A strain magnification of 500 times was used on all tests. All tests were performed at a crosshead speed of 4×10^{-3} mm sec⁻¹.

Transmission Electron Microscopy

Using transmission electron microscopy (TEM), we examined thin foils prepared from peak-aged alloys deformed in tension²⁶ at various elevated test temperatures. Specimens used for observation in TEM were initially sectioned from the gage length of tested samples, and then lapped to approximately 0.15 mm in thickness. Electrochemical thinning occurred in a dual submerged jet polisher using an electrolyte of 20% perchloric acid in ethanol at -35°C. We examined all foils in a Jeol 100C electron microscope operated at 100 kV. We used the gun tilt technique to provide our dark-field micrographs.

RESULTS AND DISCUSSIONS

Temperature Dependence of the Gamma-Gamma Prime Mismatch

Lattice constant measurements as a function of temperature yielded smooth expansion curves for all alloys. A representative thermal expansion curve for a two-phase alloy is illustrated in Figure 1. Inspection of Figure 1 shows that the coefficient of thermal expansion for the γ matrix is greater than for the γ' precipitate phase. For each alloy, we made a least squares

regression analysis for a_0^γ and $a_0^{\gamma'}$ lattice parameters versus temperature.

The thermal expansion characteristics of a γ' -strengthened, nickel-base alloy are related both to the relative amounts of γ and γ' phases present and to their respective expansion behavior. The coefficient of thermal expansion for each individual phase is a function of the composition and the type of bonding present in that phase. The alloys examined in this study were essentially two-phase alloys. The thermal expansion coefficients for both phases, the matrix (α^γ) and the γ' precipitate ($\alpha^{\gamma'}$) were determined from the alloy lattice parameters. Table III contains a complete listing of alloy expansion coefficients.

The variation of the thermal expansion coefficient of the γ matrix is analogous to that of an alloy solid solution. The expansion coefficient of a solid solution is uniquely dependent upon the types of elements present and those forces which exist between atoms in the solid solution. Morrow et al.¹⁸ have shown that Mo decreases the thermal expansion coefficient of Ni-Cr-Co γ -solid-solution alloys and wrought Ni-Cr-Al(Ti) two-phase alloys. Results presented in Fig. 2 illustrate that additions of Mo also reduce the thermal expansion coefficients of the γ matrix in Ni-Cr-Al-Ti alloys. Molybdenum has been found to partition equivalently between the γ and γ' phases in Ni-Cr-Al alloys, and to partition strongly to the γ phase in Ni-Cr-Al-Ti alloys.¹⁷ Since the thermal expansion from absolute zero to the melting point is nearly equivalent for most metals, it has been

shown²⁷ that the thermal expansion coefficient is inversely proportional to the melting point of the metal. The contribution of Mo towards lower expansion coefficients, therefore, may be due to the replacement of lower melting nickel or chromium in the matrix with higher melting molybdenum.

The thermal expansion coefficients of the γ' phase were found to be consistently smaller than those of the γ matrix. Arbuzov and Zelenkov²⁸ have suggested that the coefficient of thermal expansion of Ni_3Al is low due to the high strength of atomic bonds associated with ordered, intermetallic compounds of stoichiometric composition. A literature review of the expansion coefficients for γ' shows that the published values of $\alpha_{\gamma'}$ are entirely consistent with results obtained in this investigation for alloys 11, 15, and 6 (in situ). Alloys 11 and 15 were chosen for this comparison since they are simple Ni-Cr-Al compositions and can be assumed to contain γ' of a composition closely approximating the stoichiometric Ni_3Al phase.

Additions of alloying elements to Ni_3Al have been shown²⁸ to reduce $\alpha_{\gamma'}$ with the same element having different effects at different temperatures. The γ' expansion coefficients determined in this work exhibit a similar behavior, that is, $\alpha_{\gamma'}$ for the experimental alloys containing titanium and/or molybdenum are smaller in magnitude than the thermal expansion coefficients of alloys without these particular elements.

Values of the unconstrained γ - γ' mismatch over the temperature range 25°C to 800°C for all two-phase alloys studied are found in Table IV. Extrapolated values of the γ' lattice parameter based on established regression relationships were used in the

calculation of 700°C and 800°C γ - γ' mismatch values found in this table. As a result of the thermal expansion difference between the γ and γ' phases, alloys with a γ' lattice parameter larger than the γ lattice constant, $a_0^{\gamma'} > a_0^{\gamma}$, (that is, Type I behavior) exhibit decreasing unconstrained γ - γ' mismatch, δ , with increasing temperature. The temperature dependence of δ for alloys exhibiting Type I behavior is shown in Figs. 3 and 4. For alloys showing the reverse, that is, $a_0^{\gamma'} < a_0^{\gamma}$ (Type II behavior), the absolute value of the γ - γ' mismatch, $|\delta|$, increases slowly with increasing temperature. The variation of unconstrained mismatch with temperature for alloys 12, 13, and 14 is shown in Figure 5.

The temperature dependence of the γ - γ' mismatch for alloys 11 and 15 is unique since the misfit shifts from positive to negative values at approximately 650°C as a consequence of the thermal expansion differences of the γ and γ' phases. The temperature dependence of the misfit for alloy 11 is included in Fig. 5.

Figure 6 shows the variation between the γ' lattice parameter measured in the extracted (powder) and "in situ" conditions as a function of temperature. The proximity of the γ and γ' diffraction peaks, strain effects, and the influence of thermal diffuse scattering on weak superlattice reflections of $\text{Ni}_3\text{Al}(\text{Ti})$, precluded the determination of many γ' "in situ" lattice parameters. The observed temperature dependence of both the constrained γ - γ' mismatch, ϵ , calculated from the "in situ" data, and the unconstrained mismatch appears in Figure 7. Although the magnitudes of constrained and unconstrained mismatch differ for a particular alloy, a relative trend of decreasing misfit with increasing

temperature is exhibited for both coherency strain parameters of alloy 6 (Type I behavior). As shown in Figure 7, the rate of decrease in constrained mismatch was slightly smaller than that for the unconstrained mismatch. This is due to the thermal expansion difference measured for the γ' precipitate in the extracted and "in situ" conditions. The similar variation of ϵ and δ with temperature shows that the temperature dependence of coherency strains in the experimental alloys can be consistently represented by the unconstrained γ - γ' mismatch.

The constrained mismatch, ϵ , for fully coherent, spherical precipitates has been related to the unconstrained mismatch, δ , by:²⁹

$$\epsilon = \delta \left(\frac{1 + v}{1 + 2K + v(1 - 4K)} \right)$$

where

v = Poisson's ratio of the precipitate, and

K = the ratio: $\frac{\text{Shear modulus of the matrix}}{\text{Shear modulus of the precipitate}}$.

Substituting in representative values of $v = 0.3$ and $K = 0.9$, the above formulation simplifies to $\epsilon \approx 0.64\delta$. Over the temperature range of 25°C to 300°C, rough calculations show that this relationship is nearly constant, due in part to the invariability of the parameter K . Based on the misfit measurements for alloy 6, the same relationship of ϵ to δ was found to be $\epsilon \approx 0.79\delta$ at 25°C, changing to $\epsilon \approx 0.89\delta$ at 300°C.

Several investigations^{5,6,30} relating elevated-temperature mechanical properties to coherency strains have failed to consider the temperature dependence of the γ - γ' mismatch that arises due to the difference in the coefficients of expansion for γ and γ' . A cursory analysis by Williams³¹ inferred that coherency strains in a binary Ni-Al alloy were insensitive to temperature. Munjal and Ardell, using γ lattice parameter data of Phillips³² and the thermal expansion coefficient for γ' measured by Taylor and Floyd,³³ estimated that the γ - γ' mismatch increased with increasing temperature for a Ni-12.19 at.% Al alloy (Type I behavior). They concluded that coherency strain is strongly temperature dependent; however their misfit variation with temperature is completely different from the results in this study.

TENSILE PROPERTIES

Temperature Dependence of the Flow Stress for the Single-Phase Control Alloys

We used elevated temperature tensile tests to measure the flow stress as a function of temperature of the single-phase, control alloys 16, 17, and 18. The temperature dependence of the 0.2% flow stress for the control alloys is shown in Figure 8. Each control alloy exhibits a continuously decreasing flow stress with increasing temperature; this flow stress behavior is characteristic of single-phase, face-centered cubic metals.

Alloys 16 and 18 display comparable yield strengths at room temperature; however alloy 16 exhibits a smaller decrease in flow strength between 25°C and 800°C. The strength of alloy 17 decreases with increasing temperature at approximately the same rate as a Ni-8 at.% Al solid solution alloy tested by Davies and Stoloff.³⁴ Alloys 16 and 17 show very similar temperature dependencies of their flow stresses over the temperature range of interest. Alloy 17 exhibits the smallest flow stress of the three control alloys at all test temperatures. The room temperature flow stress of alloy 17, $\sigma_y(25^\circ\text{C}) = 162 \text{ MPa}$, is very similar to the solutionized flow stress of alloy 11, $\sigma_{ss}(25^\circ\text{C}) = 173 \text{ MPa}$. Both alloy 11 and 17 have similar compositions.

Yielding Behavior of the Peak-Aged Alloys as a Function of Temperature

The temperature dependence of the flow stress for each control alloy provides an estimate of the properties of the γ' -strengthened alloys in the solutionized condition. Flow stress data for the control alloys in conjunction with existing peak-aged flow stress data for the two-phase experimental alloys,^{8,26} allows the increment in flow stress due to precipitation of γ' to be calculated as a function of temperature. Using the room temperature solutionized flow stress, σ_{ss} , measured for each experimental alloy, and the temperature variation of the flow stress for the appropriate control alloy composition, a flow stress versus temperature estimate was determined for each alloy. The increment in yield stress

due to precipitation, $\Delta\sigma_y$, as a function of temperature, was then taken as the difference between γ_y max. and the adjusted control alloy flow stress, σ_y .

The variation in flow stress increments of alloys 1-3, and 8-13 with $\gamma-\gamma'$ mismatch, δ , for the temperature range 25°C to 300°C is illustrated in Figure 9. The $\gamma-\gamma'$ mismatch of these alloys was altered either by adding molybdenum at constant Ti/Al ratio, or by varying the Ti/Al ratio. The (Ti+Al) content is constant at 7 atomic percent in these alloys. The flow stress increments for alloys 3, 8, 1 and 11 exhibit a linear behavior with $\gamma-\gamma'$ mismatch over the temperature range of interest. The linear relationship for these alloys is indicated in Figure 9. Alloys 3, 8, 1 and 11 were designed to provide large mismatch variations as the Ti/Al ratio increased from 0 to 5.4. Small differences in weight fraction of γ' exist among these alloys.⁸

A large influence of γ' weight fraction can be seen in the flow stress increments determined for alloys 11, 12, and 13. The values of $\Delta\sigma_y$ for these alloys increase significantly as the weight fraction of γ' nearly doubles between alloy 11 and 13.⁸

Alloys 1, 2, 9, and 10 designed for varying $|\delta|$ at constant Ti/Al ratio, exhibit increasing flow stress increments as $|\delta|$ increases. Additions of molybdenum, which are used to alter $|\delta|$, bring about a systematic increase in the γ' weight fraction causing a departure from linearity among these alloys.

The contribution of coherency strains to alloy strengthening over the temperature interval 25°C to 800°C can be better illustrated by correcting the flow stress increments for the differences

in the weight fraction of γ' that exist in alloys 1-3, and 8-13. This correction is valid since the empirical, linear relationship between the flow stress increment and the weight fraction of γ' determined for room temperature data⁸ can be shown to exist for elevated temperature behavior as well. This linear relation between the flow stress increments and fraction of γ' at constant $\gamma-\gamma'$ misfits is shown in Figure 10 for 200°C to 800°C yield stress data. Alloys 11, 12, and 13, in which the magnitude of the $\gamma-\gamma'$ mismatch is low and the $|\delta|$ variance is small, exhibit a good linear correlation of $\Delta\sigma_y$ with weight fraction γ' at each temperature. For these particular alloys, we noted a small drop in the slope of this linear behavior at 800°C. The increase in $\Delta\sigma_y$ with weight fraction of γ' is also linear in alloys 3 through 6, with the linear correlation degenerating slightly as the test temperature increases. Although the linear correlation established for high mismatch alloys at 400°C to 800°C is less than that found at lower temperatures, the errors introduced by a linear correction of $\Delta\sigma_y$ should be minor due in part to the small weight fraction variation existing in alloys 1-3, and 8-13.

The values of the 25°C to 300°C normalized flow stress increments, $\Delta\sigma_y / (\text{wgt. \% } \gamma')$, for alloys 1-3 and 8-13 are plotted against the unconstrained $\gamma-\gamma'$ mismatch in Figure 11. Regression analysis of the data contained in this master plot indicates that the best regression model for the increment in alloy flow stress due to γ' precipitation and the measured coherency strains is that of a linear proportionality. Miller and Ansell⁸ have reported a similar

linear association of the variables $\Delta\sigma_y/\text{wgt. \% } \gamma'$ and $|\delta|$ for the room temperature mechanical behavior of these alloys.

The greatest degree of data scatter found in the linear relationship shown in Figure 11 is exhibited by Group C and D alloys, specifically the low or near zero mismatch alloys 9 through 13. A linear fit of the data for high misfit alloys is significantly better than that found for low $\gamma-\gamma'$ misfit alloys of Groups C and D. Figure 12 is a replot of $\Delta\sigma_y/\text{wgt. \% } \gamma'$ versus $|\delta|$ data taken from Figure 11 for Group A and B alloys. Provided that the antiphase boundary energy of γ' is related to the Ti/Al ratio, large changes in APBE should exist between Group A and B alloys. Nevertheless, the excellent correlation of the normalized increment in flow stress with $\gamma-\gamma'$ mismatch for the 25°C to 800°C yield data indicates that strengthening in these high misfit alloys results primarily from coherency strains. Conversely, the influence of other strengthening mechanisms, namely order of strengthening, is expected to become more dominant as the magnitude of $\gamma-\gamma'$ mismatch is decreased; the deviation from linearity seen for Groups C and D alloys is taken as evidence of this behavior.

A large difference in antiphase boundary energy has been measured⁸ between Group C alloy 10 and Group D alloy 11. The relative, quantitative relationship in antiphase boundary energy that exists between Groups C and D is supported by the variation in normalized flow stress increments reported in Figure 11, that is, the $\Delta\sigma_y/\text{wgt. \% } \gamma'$ value for alloys 9 and 10 are greater than for Group D alloys 11, 12, and 13.

DISLOCATION - PARTICLE INTERACTIONS

We used transmission electron microscopy to characterize and contrast dislocation substructures of Groups A, B, C, and D. Selected alloys, namely alloys 1, 8, 10, 11, and 13 were examined. Contrasting the deformation behavior of Groups A and B with Groups C and D allows one to discern the relative influence of the γ - γ' mismatch. The effect of large measured differences in antiphase boundary energy at low coherency strains can be obtained by analyzing structures of Group C alloy 10 and Group D alloy 11. The deformation behavior of Group D alloy 13 is representative of a low APBE, negative misfit alloy.

Group D Deformation Substructures

The slip behavior observed in alloy 11 deformed at 200°C is predominantly planar, typical of alloys possessing coherent, ordered particles. Dislocations found in alloy 11 at this test temperature are generally paired indicating some type of particle shear.³⁵ A large number of massive shear bands, Figure 13, was observed in this alloy substantiating the existence of particle shear.

The deformation character of alloy 11 tested at 400°C remained planar, with paired dislocations and shear bands dominating the observed structures as shown in Figure 14. Close examination of Figure 14 (arrow) indicates that the observed pairs of superlattice

dislocations may be a more complex equivalent dislocation configuration. Superlattice dislocations in an $L1_2$ structure tend to consist of pairs of $a/2 <110>$ -type dislocations coupled together by antiphase boundary. Marcinkowski et al.³⁶ suggested that each $a/2 <110>$ dislocation can itself be dissociated into a pair of Shockley partials coupled by a complex fault, which corresponds to the sum of an antiphase boundary and a stacking fault. Using high resolution weak beam dark field techniques, we observed what was initially believed to be evidence of a dislocation configuration comprised of four partial dislocations in this alloy (see Figure 15). The equilibrium width of such a dissociated superlattice dislocation is determined by the balance between the tensions exerted by the faults and the repulsive forces experienced by the constituent partial dislocations. Calculated values for separation of the partial dislocations constituting a dislocation pair in an $L1_2$ superlattice have been made by Marcinkowski, et al., in terms of antiphase boundary energy and stacking fault energy. Calculations indicate that partial separation would be extremely small, and hence resolution of the individual partials would not be expected. Figure 15 is more likely an example of a double superlattice dislocation array,³⁷ that is, images produced by two distinct superlattice dislocations lying parallel and close to each other.

The unconstrained $\gamma-\gamma'$ mismatch measured for alloy 11 is unique in that this misfit parameter changes from a positive to a negative value at approximately 650°C. The structure found in alloy 11 deformed at 800°C was generally more homogeneous than that detected

at lower deformation temperatures in the same alloy. Foils examined illustrate that at 800°C a greater number of individual dislocations were present. A slightly higher density of residual dislocation loops surrounding γ' precipitates was noted. Nevertheless, numerous paired dislocations were observed, thus indicating that smaller particles were still being sheared.

In addition to Group D alloy 11, foils taken from tensile specimens of alloy 13 tested at 600°C and 800°C were examined by TEM in order to discern any effect on dislocation-particle interactions due to negative coherency strains. The γ - γ' mismatch of alloy 13 was negative at all test temperatures, varying from -0.14% at 25°C to -0.25% at 800°C.

Several other Burgers vector analyses were conducted on foils taken from alloy 13 tested at 600°C. In addition to observing superlattice pairs of the type $a/2 <110>$, a few net Burgers vectors of the type $a <112>$ were also identified by examining the dislocation contrast from various two-beam diffraction conditions.

Figure 16 illustrates isolated pairs of dislocations observed in alloy 13. Minor evidence of superlattice intrinsic/extrinsic stacking fault contrast in the γ' particles appears (see arrow) in the weak beam dark field micrograph, Figure 16b. A closely spaced double superlattice dislocation array is also imaged in Figure 16.

The dislocation structure of alloy 13 tested at 800°C was less planar in nature, Figure 17, than that found in 600°C-deformed specimens. A higher degree of individual dislocations was observed; however dislocation pairing with significant bowing of the lead dislocation was still evident. Relative to alloy 10, few superlattice intrinsic/extrinsic stacking faults in the γ' were found, and

the number of residual loops observed was modest. In general, the deformation behavior of alloy 13 tested at 800°C was more homogeneous than that found in 600°C tensile specimens.

Group C Dislocation - Particle Interactions

Group C tensile behavior is represented by dislocation-particle interactions observed in alloy 10. In tensile specimens deformed at 200°C, we observed planar arrays of paired dislocations and evidence of production of stacking faults within the ordered γ' precipitates. Evidence of individual γ' particles supporting double coplanar, residual dislocation loops was also found in alloy 10 tested at 200°C; see Figure 18.

Experimental evidence³⁸ has been presented for the existence of superlattice intrinsic (or extrinsic) stacking fault type particle shearing mechanisms in nickel-base alloys deformed at high strain rates. Figure 19 illustrates the image contrast variation in the + \bar{g} and - \bar{g} diffracting conditions arising from this type stacking faults found in alloy 10. Due to the high antiphase boundary energy of alloy 10, alternative shear mechanisms involving dissociation of a pair of superlattice dislocations into partials coupled by a relatively low energy intrinsic (or extrinsic) stacking fault configuration must become competitive.

Examination of foils of alloy 10 tested at 400°C and 600°C also showed planar arrays of paired dislocations. The weak beam dark field technique using superlattice reflections provided

evidence of shear of the γ' particles. Superlattice intrinsic/extrinsic stacking faults in the γ' precipitates were also observed.

In alloy 10 specimens deformed at 800°C, superlattice intrinsic/extrinsic stacking fault contrast was still evident; see Figure 20. Figure 21 shows that dislocation motion at this temperature was likewise found in pairs with large numbers of residual dislocation loops found on primary slip planes.

The existence of matrix stacking faults indicates that alloy 10 possesses a low matrix stacking fault energy. A low stacking fault energy γ matrix is characteristic of many nickel-base alloys. Alloying elements that partition preferentially to the γ phase, such as Co, Mo and particularly Cr, reduce the stacking fault energy of nickel.³⁹⁻⁴¹ Kear and Oblak⁴² have pointed out that an important consequence of lowered matrix stacking fault energy is that certain dissociated dislocations in the γ matrix can, in fact, experience a short-range attraction. This is because the constituent partial dislocations can arrange themselves as intrinsic/extrinsic fault pairs, thus providing a perfect translation vector for shearing γ' particles.

Group A Deformation Structures

The deformation substructures observed in alloy 1 exemplify the behavior of high misfit Group A alloys. The dislocation substructure of alloy 1 was found to be predominantly planar, exhibiting multiple slip intersections of dislocation bands at all test

temperatures, as in Figure 22. Dislocations were found to be tangled within well-defined slip bands indicating a strong interaction between the moving dislocations and the γ' particles. A very low degree of paired dislocations was observed, and no evidence of particle shear was found. The observed deformation character of alloy 1 varied little as a function of temperature. However, foils sectioned from 800°C tensile specimens showed many fields of pinched off dislocation loops, Figure 23, in contrast to specimens deformed at lower test temperatures. Due to the strain field contrast around the γ' precipitates which occurs as a result of the large γ - γ' mismatch found at all test temperatures in alloy 1, it was difficult to image dislocation at or near the γ - γ' interface.

DISCUSSION AND SUMMARY OF TENSILE DISLOCATION - PARTICLE INTERACTIONS AND YIELDING BEHAVIOR

Direct evidence of particle shear was observed in low misfit Group C and D alloys. Group D alloy 11 exhibited faulting of the γ' by coupled pairs of superlattice dislocations corresponding to shear displacement of the type $a/2 <110>$. In contrast, shear of the ordered γ' in Group C alloy 10 was characterized by the production of intrinsic/extrinsic stacking faults.

Dislocation-particle substructures of Group A alloy 1 showed neither evidence of particle shear nor characteristic arrays of paired dislocations. The intersection and entanglement of dislocations within well-defined slip bands, Figure 22, indicates a strong interaction between dislocations and γ' particles exists in Group A alloys due to coherency strains. Although the γ - γ' mismatch decreases with increasing temperature in alloy 1, the

misfit remains large at 800°C. As a result, particle by-pass clearly dominates particle shear even at 800°C, as illustrated by the bands of dislocation loops in Figure 23. It is clear from the present evidence that the mechanism of yield in Group A alloys resembles an Orowan-type process, whereas particle shear predominates in Group C and D alloys. The diverse deformation modes observed between Group A and Groups C and D substantiate the influential role of coherency strains on resultant dislocation-particle interactions.

Even though evidence of particle shear was observed in both low misfit Group C and D alloys, the nature of the particle shear in each group was extremely distinctive. Foils of Group D alloy 11 exhibited γ' sheared mainly by $a/2 <110>$ superlattice dislocations coupled together by antiphase boundary. The equilibrium width of dislocation pairs in nickel-base alloys is sensitive to APBE; the lower the APBE, the wider the dislocation separation. In addition, each dislocation of the pair is likely to be dissociated into a pair of Shockley partials coupled together by complex fault.³⁶ Calculations have shown⁴² that the extent of the dissociation of the Shockley partials in stoichiometric Ni₃Al is only ~ 0.5 nm, and therefore not ordinarily resolved in transmission electron microscopy.

In contrast to deformation structures found in Group D, slip in the high antiphase boundary energy Group C alloy 10 involved the creation of superlattice intrinsic/extrinsic stacking faults; see Figures 19 through 21. Alloy 10 is exemplary of a low mismatch

alloy in which the stability of residual dislocation loops is expected to be determined primarily by the APBE of γ' . The support of a double residual dislocation loop by a single γ' particle, shown in Figure 18, is taken as evidence for high APBE of the γ' phase in alloy 10.

Evidence of superlattice intrinsic/extrinsic stacking fault shear has been found in nickel-base alloys deformed at high strain rates.³⁸ Calculations by Kear and Oblak⁴² indicate that dissociations producing configurations of partial dislocations coupled together by complex intrinsic/extrinsic stacking faults become competitive with high APB-type shear in materials with high anti-phase boundary energy. Furthermore, alloying additions such as Mo, Ti and Al, have been found to reduce the stacking fault energy of nickel,³⁹⁻⁴¹ thus favoring the arrangement of certain γ matrix dissociated dislocations into intrinsic/extrinsic fault pairs that constitute a perfect translation vector for shearing γ' particles.⁴² It is therefore difficult to discern unequivocally whether the high APBE or the lowered stacking fault energy of the matrix in Group C alloys is the controlling factor for the observed intrinsic/extrinsic stacking fault type shear.

Copley and Kear⁴³ have proposed a dynamic theory of coherent precipitation hardening that accounts for the increase in the yield strength of the high volume fraction, low misfit alloy, Mar-M200. The dominant strengthening contribution for the resolved shear stress comes from the antiphase boundary energy, or more precisely the fault energy of γ' . Four basic types of faults in γ' must be considered, that is, complex fault, antiphase boundary, superlattice

intrinsic fault (S-ISF), and superlattice extrinsic fault (S-ESF). Kear, et al,⁴⁴ point out that at a given temperature, the major contribution to the shear stress in this model may be determined by the fault of least energy. The energy scheme predicted by Kear, et al,⁴⁴ CF>APB>(S-ESF)>(S-ISF), seems reasonable in light of the observed deformation structures in the high antiphase boundary energy Group C alloys.

Dislocation pair behavior analogous to that shown in Figure 16 has been described by Nam and Brown.¹⁰ In alloys with small, ordered precipitates, both dislocations remain straight. For larger particles at peak aging, the lead dislocation bows as it samples regions of adverse stress, while the trail dislocation remains straight. Since the antiphase boundary energy of alloy 13 should be low,³ the lead dislocation is expected to penetrate the γ' particle prior to any significant bowing by the trail dislocation. The observed paired dislocation arrangements shown in Figure 16 and the absence of residual dislocation loops are consistent with this mechanism.

Group D alloy 13 and Group C alloy 10 represent low coherency strain alloys. The degree of hardening and the associated deformation behavior should be influenced markedly by the antiphase boundary energy of γ' , or as Kear et al.⁴⁴ have suggested, by the fault of least energy. Relatively few superlattice intrinsic/extrinsic type faults were observed in alloy 13 in contrast to alloy 10. The stacking fault energy of alloy 13 is expected to be low, based on the reported³⁹ influence of titanium, aluminum, and molybdenum on stacking fault densities in nickel.

Since titanium and molybdenum are more potent than aluminum in reducing the stacking fault energy of nickel, the stacking fault energy of alloy 10 should be lower than that for alloy 13. The high APBE and low stacking fault energy of alloy 10 suggests that intrinsic/extrinsic faults are the lower energy fault in this particular alloy. Conversely, the low APBE and slightly greater stacking fault energy of alloy 13 implies that the relative energy difference between intrinsic/extrinsic and APB faults is small in this alloy. The deformation behavior exhibited by alloy 13 is consistent with this observation. This suggests that alloying additions such as titanium and molybdenum, which decrease the matrix stacking fault energy, can have a significant effect on the relative energies of intrinsic/extrinsic faults with respect to antiphase boundary, and therefore influence the deformation character.

The structure-flow stress relationships established for Groups C and D delineate the weak dependence of alloy strength on coherency strains in low misfit alloys. Raynor and Silcock⁹ have concluded from their study of γ' -strengthened austenitic steels that strengthening in alloys with low $\gamma-\gamma'$ mismatch is attributable to the APBE of γ' . The diverse deformation structures observed in Group C and D alloys suggest that the relationship of APBE to alternative fault energies is extremely important in determining the yielding behavior in low coherency strain Ni-Cr-Al-Ti-Mo alloys.

In alloys studied at low or intermediate temperatures, several investigators have shown that coherency strains caused by

mismatch between the precipitate and matrix lattice parameters enhance the strength obtained from a dispersion of coherent particles. The dependence of alloy strength on the magnitude of γ - γ' mismatch found in this investigation is consistent with the results of Mihalisin and Decker,^{3,4} Parker,⁴⁵ and Miller and Ansell. The linear dependence of $\Delta\sigma_y/\text{wgt.\% } \gamma'$ and γ - γ' lattice mismatch over the temperature range 200°C to 800°C substantiates the role of coherency strain strengthening found in the low temperature study⁸ of this experimental nickel-base alloy series.

A generalized summary of the yielding behavior observed in this study is provided in Figure 24. Derived structure-property relationships permit high and low coherency strain alloys of the Ni-Cr-Al-Ti-Mo system to be recapitulated in the manner illustrated.

Coherency strains were found to be the principal determinant of tensile strength in high misfit alloys over the temperature range investigated. The excellent correlation of the increment in flow stress to γ - γ' mismatch and the associated dislocation-particle interactions observed in TEM support this finding. In near zero mismatch alloys, the influence of coherency strain strengthening is insignificant, as illustrated by the predominance of γ' particle shearing. In contrast, high misfit alloys exhibit particle by-pass dislocation behavior regardless of the magnitude in APBE.

CONCLUSIONS

1. The constrained and unconstrained γ - γ' mismatch have analogous temperature dependencies, indicating that the unconstrained

γ - γ' misfit is a consistent representation of coherency strain behavior.

2. A linear relationship exists between the strengthening of γ - γ' alloys after accounting for differences in the weight fraction of γ' and the unconstrained γ - γ' mismatch over the temperature range 25°C to 800°C. The linear correlation is strongest for high misfit alloys regardless of the APBE.
3. The magnitude of coherency strain in Ni-15Cr-Al-Ti-Mo alloys appears to determine the intrinsic dislocation-particle interactions. Deformation substructures observed in TEM in high misfit alloys exhibit by-pass type dislocation-particle structures. In contrast, low coherency strain alloys exhibit two distinct particle shear mechanisms that are believed to be dependent upon the relative APBE and stacking fault energy of the alloy.

ACKNOWLEDGEMENT

This work was supported by the Office of Naval Research and was performed at the NASA Interdisciplinary Materials Research Center at Rensselaer Polytechnic Institute.

REFERENCES

1. G. R. Stoeckinger and J. P. Neumann: J. Appl. Cryst., 1970, vol. 3, p.32.
2. Rolf Nordheim and Nicholas J. Grant: Trans. AIME, 1954, vol. 20, p.211.
3. J. R. Mihalisin and R. F. Decker: Trans. AIME, 1960, vol. 218, p. 507.
4. R. F. Decker and J. R. Mihalisin: Trans. ASM, 1969, vol. 62, p. 481.
5. I. I. Mirkin and O. D. Kancheev: Met. Sci. Heat Treat., 1967, nos. 1 and 2, p. 10.
6. G. N. Maniar and J. E. Bridge: Met. Trans., 1971, vol. 2, p. 95.
7. L. B. Pfeil, H. P. Allen and C. G. Conway: High Temperature Steels and Alloys for Gas Turbines, Spec. Rept. No. 43, Iron Steel Inst., London, 1951.
8. R. F. Miller and G. S. Ansell: Met. Trans. A, 1977, vol. 8A, p. 1979.
9. D. Raynor and J. M. Silcock: Met. Sci. J., 1970, vol. 4, p. 121.
10. L. M. Brown and R. K. Ham: Strengthening Methods in Crystals, A. Kelly and R. B. Nicholson, eds., p. 62, Applied Science Pub., Ltd., 1971.
11. N. S. Stoloff: The Superalloys, C. Sims and W. C. Hagel, eds., p. 79, Wiley, 1972.
12. V. A. Phillips: Scripta Met., 1968, vol. 2, p. 147.

13. J. M. Oblak, D. F. Paulonis and D. S. Duvall: Met. Trans., 1974, vol. 5, p. 143.
14. V. Munjal and A. J. Ardell: Acta Met., 1975, vol. 23, p. 513.
15. A. J. Ardell, V. Munjal and D. J. Chellman: Met. Trans. A, 1976, vol. 7A, p. 1263.
16. J. W. Goodrum and E. G. Lefevre: Met. Trans. A., 1977, vol. 8A, p. 939.
17. W. T. Locmis, J. W. Freeman and D. L. Sponseller: Met. Trans., 1972, vol. 3, p. 989.
18. H. Morrow, D. L. Sponseller and M. Semchyshen: Met. Trans. A, 1975, vol. 6A, p. 477.
19. O. H. Kriegé and J. M. Baris: Trans. ASM, 1969, vol. 62, p. 195.
20. C. H. Kriegé and C. P. Sullivan: Trans. ASM, 1968, vol. 61, p. 278.
21. R. F. Miller: Ph. D. Thesis, Rensselaer Polytechnic Institute, 1977.
22. M. J. Donachie and O. H. Kriegé: J. Materials, 1972, vol. 7, p. 269.
23. D. D. Cullity: Elements of X-Ray Diffraction, p. 324, Addison-Wesley Pub. Co., 1967.
24. R. D. Simmons and R. W. Dalluffi: Phys. Rev., 1962, vol. 125, p. 862.
25. W. D. Pearson: Lattice Spacing and Structure of Metals and Alloys, Pergamon Press, 1958.
26. M. W. Broadley: M. S. Thesis, Rensselaer Polytechnic Institute, 1979.

27. C. Zwikker: Physical Properties of Solid Materials, p. 159, Interscience, 1954.
23. M. P. Arbuzov and I. A. Zelenkov: Phys. of Metals and Metallography, 1963, vol. 16, p. 65.
29. G. R. Woolhouse and L. M. Brown: J. Inst. Metals, 1970, vol. 98, p. 106.
30. G. N. Maniar, J. E. Bridge, H. M. James and G. E. Heydt: Met. Trans., 1970, vol. 1, p. 31.
31. R. O. Williams: Trans. AIME, 1959, vol. 215, p. 1026.
32. V. A. Phillips: Phil. Mag., 1967, vol. 16, p. 103.
33. A. Taylor and R. W. Floryd: J. Inst. Metals, 1952-1953, vol. 81, p. 25.
34. R. G. Davies and N. S. Stoloff: Trans. AIME, 1965, vol. 233, p. 714.
35. H. Gleiter and E. Hornbogen: Phys. Status Solidi, 1965, vol. 12, p. 235.
36. M. J. Marcinkowski, N. Brown and R. M. Fisher: Acta Met., 1961, vol. 9, p. 129.
37. D. G. Morris and R. E. Smallman: Acta Met., 1975, vol. 23, p. 73.
38. L. R. Cornwell, G. R. Purdy and J. D. Embury: Phys. Status Solidi, 1969, vol. 35, p. K1.
39. L. Delehouzee and A. Deruyhere: Acta Met., 1967, vol. 15, p. 727.
40. E. E. P. Feeston, I. L. Dillamore and R. E. Smallman: Metal Sci. J., 1968, vol. 2, p. 12.

41. E. E. P. Beeston and L. K. France: J. Inst. Metals, 1963, vol. 96, p. 105.
42. B. H. Kear and J. M. Oblak: J. de Physique, Colloque C7, 1974, vol. 35, suppl. no. 12, p. C7-35.
43. S. M. Copley and B. H. Kear: Trans. AIME, 1967, vol. 239, p. 984.
44. B. H. Kear, A. F. Giamei, J. M. Silcock and R. K. Ham: Scripta Met., 1968, vol. 2, p. 237.
45. B. A. Parker: Scripta Met., 1970, vol. 4, p. 905.

Table I
Alloy Groups Based Upon General Coherency Strain
and APBE Properties

Group Designation	Alloy Numbers	General Properties	$\gamma - \gamma'$ Mismatch Range at 25°C	Ti/Al Ratio (APBE)
Group A	1, 2, 3	• High Coherency Strain	$0.77 < \delta < 1.04\%$	Ti/Al=1.8
	4-7	• High APBE		
Group B	8	• High Coherency Strain • Low APBE	$\delta = 0.56\%$	Ti/Al=0.5
	9, 10	• Low Coherency Strain • High APBE	$\delta (9) = 0.44\%$ $\delta (10) = 0.16\%$	Ti/Al=1.8 $\gamma_{APB} (10) = 0.2 J m^{-2}$
Group D	11-15	• Low Coherency Strain • Low APBE	$-0.14 < \delta < 0.06\%$	Ti/Al=0 $\gamma_{APB} (11) = 0.133 J m^{-2}$
	16, 17, 18	• Control - Non-Precipitation hardenable	N.A.	N.A.

Table II
Actual Composition of the Experimental Alloy*
 (atomic %)

<u>Alloy</u>	<u>Cr</u>	<u>Mo</u>	<u>Al</u>	<u>Ti</u>	<u>B</u>	<u>C</u>
1	14.99	0	2.42	4.47	0.026	0.248
2	15.09	0.99	2.52	4.51	0.026	0.212
3	15.09	0	1.09	5.36	0.026	0.207
4	15.11	0.15	2.71	4.45	0.026	0.198
5	15.14	0.52	2.90	4.54	0.026	0.201
6	14.73	0.12	3.13	5.11	0.026	0.201
7	15.06	0.37	3.37	5.64	0.026	0.205
8	15.15	0	4.68	2.29	0.031	0.199
9	15.11	2.96	2.49	4.46	0.032	0.258
10	15.11	4.98	2.56	4.48	0.027	0.271
11	15.12	0	6.94	0	0.026	0.226
12	15.09	2.97	7.07	0	0.026	0.197
13	14.51	4.99	7.12	0	0.032	0.214
14	14.39	4.38	7.10	0	0.024	0.478
15	14.74	0	10.18	0	0.021	0.324
16	15.09	4.98	0	0	0.027	0.198
17	15.23	0	3.19	0	0.025	0.047
18	15.05	0	1.52	2.52	0.026	0.157

Typical Trace Analysis Excluding Above Additions (wt.%)

Mn	P	S	Si
0.003	0.0003	0.001	0.040

*Balance nickel

Table III
Coefficients of Thermal Expansion, α in $^{\circ}\text{C}^{-1}$
For the Experimental Alloys

<u>Alloy</u>	α^Y (25°C to 800°C)	α^Y (25°C to 600°C)
1	1.63×10^{-5}	1.26×10^{-5}
2	1.70×10^{-5}	1.26×10^{-5}
3	1.63×10^{-5}	1.26×10^{-5}
4	1.70×10^{-5}	1.26×10^{-5}
5	1.74×10^{-5}	1.26×10^{-5}
6	1.74×10^{-5}	1.26×10^{-5}
		$1.44 \times 10^{-5}^{*+}$
7	1.70×10^{-5}	1.26×10^{-5}
8	1.67×10^{-5}	1.41×10^{-5}
9	1.59×10^{-5}	1.22×10^{-5}
10	1.48×10^{-5}	1.26×10^{-5}
11	1.67×10^{-5}	1.42×10^{-5}
12	1.48×10^{-5}	1.32×10^{-5}
13	1.48×10^{-5}	1.27×10^{-5}
14	1.52×10^{-5}	$1.34 \times 10^{-5}^{*+}$
15	1.63×10^{-5}	$1.37 \times 10^{-5}^{**}$
16	1.63×10^{-5}	N.A.

* Calculated based upon 25°C to 800°C data.

** Calculated based upon 25°C to 700°C data.

+ In situ.

Table IV

Unconstrained $\gamma-\gamma'$ Mismatch, δ for
the Temperature Range 25°C to 800°C

	Alloy	Temperature in °C				
		25°C	200°C	400°C	600°C	700°C
Type I Behavior	1	0.0093*	0.0090	0.0084	0.0075	0.0070†
	2	0.0079*	0.0070	0.0061	0.0058	0.0053†
	9	0.0042*	0.0039	0.0036	0.0033	0.0025†
	10	0.0017*	0.0017	0.0014	0.0008	0.0004†
	8	0.0059*	0.0062	0.0059	0.0053	0.0047†
	3	0.0104*	0.0098	0.0092	0.0086	0.0082†
	4	0.0090*	0.0084	0.0073	0.0067	0.0063†
	5	0.0090*	0.0087	0.0084	0.0072	0.0063†
	6	0.0090†	0.0078	0.0070	0.0061	0.0057†
	6 in situ	0.0070*	0.0062	0.0056	0.0050	0.0047
$(a_o^{\gamma'} > a_c^{\gamma})$	7	0.0093*	0.0090	0.0078	0.0070	0.0065†
	11	-0.0006*	-0.0006	-0.0006	-0.0006	-0.0010†
	12	-0.0014	-0.0011	-0.0014	-0.0019	-0.0020†
	13	-0.0008	-0.0011	-0.0011	-0.0017	-0.0019
	14	-0.0008	-0.0011	-0.0011	-0.0017	-0.0022
Type II Behavior	11	0.0006*	0.0011	0.0011	0.0006	-0.0006†
	15	0.0003	0.0008	0.0003	-0.0003	-0.0008

* Reference 8.

† Calculation based on extrapolated $a_o^{\gamma'}$ data.

FIGURE CAPTIONS

Figure 1 - Lattice constants of the γ matrix and γ' precipitate vs temperature for alloy 14.

Figure 2 - Coefficient of thermal expansion vs Mo content for the γ phase.

Figure 3 - The unconstrained γ - γ' mismatch, δ , as a function of temperature for alloys, which exhibit Type I behavior.

Figure 4 - Unconstrained γ - γ' mismatch, δ , as a function of temperature for Type I alloys 4 through 7.

Figure 5 - Variation of γ - γ' mismatch as a function of temperature for Type II alloys.

Figure 6 - Lattice parameter as a function of temperature for extracted and "in-situ" γ' from alloy 6.

Figure 7 - Variation in unconstrained and constrained γ - γ' mismatch with temperature for alloy 6.

Figure 8 - The 0.2% yield stress (σ_y) versus temperature for control alloys.

Figure 9 - Flow stress increment, $\Delta\sigma_y$, vs γ - γ' mismatch, $|\delta|$, for alloys 1-3, 8-13 over the temperature range 25°C to 800°C. 25°C data from reference 8.

Figure 10 - Flow stress increment, $\Delta\sigma_y$, vs weight fraction of γ' for temperature interval 200°C to 800°C.

Figure 11 - Normalized flow stress increment vs $\gamma-\gamma'$ mismatch over the temperature range 25°C to 800°C for alloys 1-3, 8-13. 25°C data from reference 8.

Figure 12 - Replot of normalized increment in yield stress, $\Delta\sigma_y/\text{wgt. \% } \gamma'$, against $\gamma-\gamma'$ mismatch for high misfit alloys 1, 2, 3, and 8. 25°C data from reference 8.

Figure 13 - γ' particle shear in alloy 11 tensile tested at 200°C.
a) Bright-field image of shear band and selected area diffraction pattern, and;
b) Dark-field image of γ' precipitates ($\bar{g} = 0\bar{1}0$), (Z.A. = 110).

Figure 14 - Dislocation structure of alloy 11 tested at 400°C.
Paired dislocations formed by 2% tensile strain ($\bar{g} = 200$), (Z.A. = 001).

Figure 15 - Double superlattice dislocation arrays observed in alloy 11 tested at 400°C.
a) Bright-field image of dislocation arrays;
b) Weak beam dark field image ($\bar{g} = 020$), (Z.A. = 110).

Figure 16 - Dislocation structures in alloy 13 deformed in tension at 600°C.
a) Bright-field image; b) Dark-field image of dislocations ($\bar{g} = 0\bar{2}0$), (Z.A. = 110).

FIGURE CAPTIONS
(cont'd)

Figure 17 - Homogeneous deformation behavior of alloy 7, deformed 2% in tension at 800°C.

Figure 18 - Paired dislocations and double dislocation loops in alloy 10 tested at 200°C.

Figure 19 - Influence of reversing \bar{g} on dislocation and intrinsic/extrinsic stacking fault images in alloy 10. Deformed 2% in tension at 200°C.
a) Image contrast for $+ \bar{g} = 11\bar{1}$, Z.A. = 112,
b) Contrast shift for diffracting vector $- \bar{g} = 11\bar{1}$.

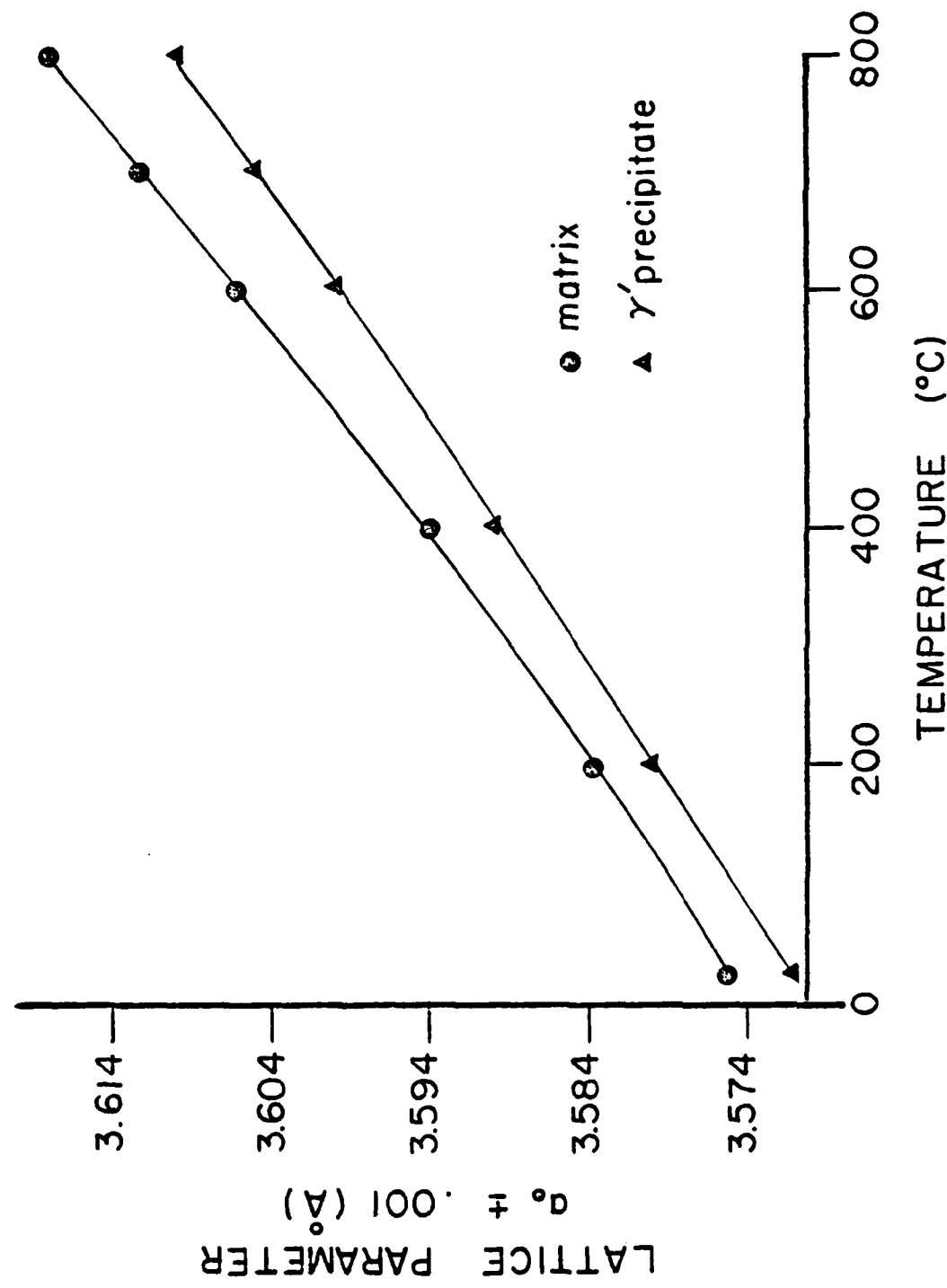
Figure 20 - Intrinsic/extrinsic faults in γ' particles of alloy 10 deformed at 800°C.
a) Bright-field image of faulted γ' particles.
b) Dark-field image ($\bar{g} = 020$), (Z.A. = 110).

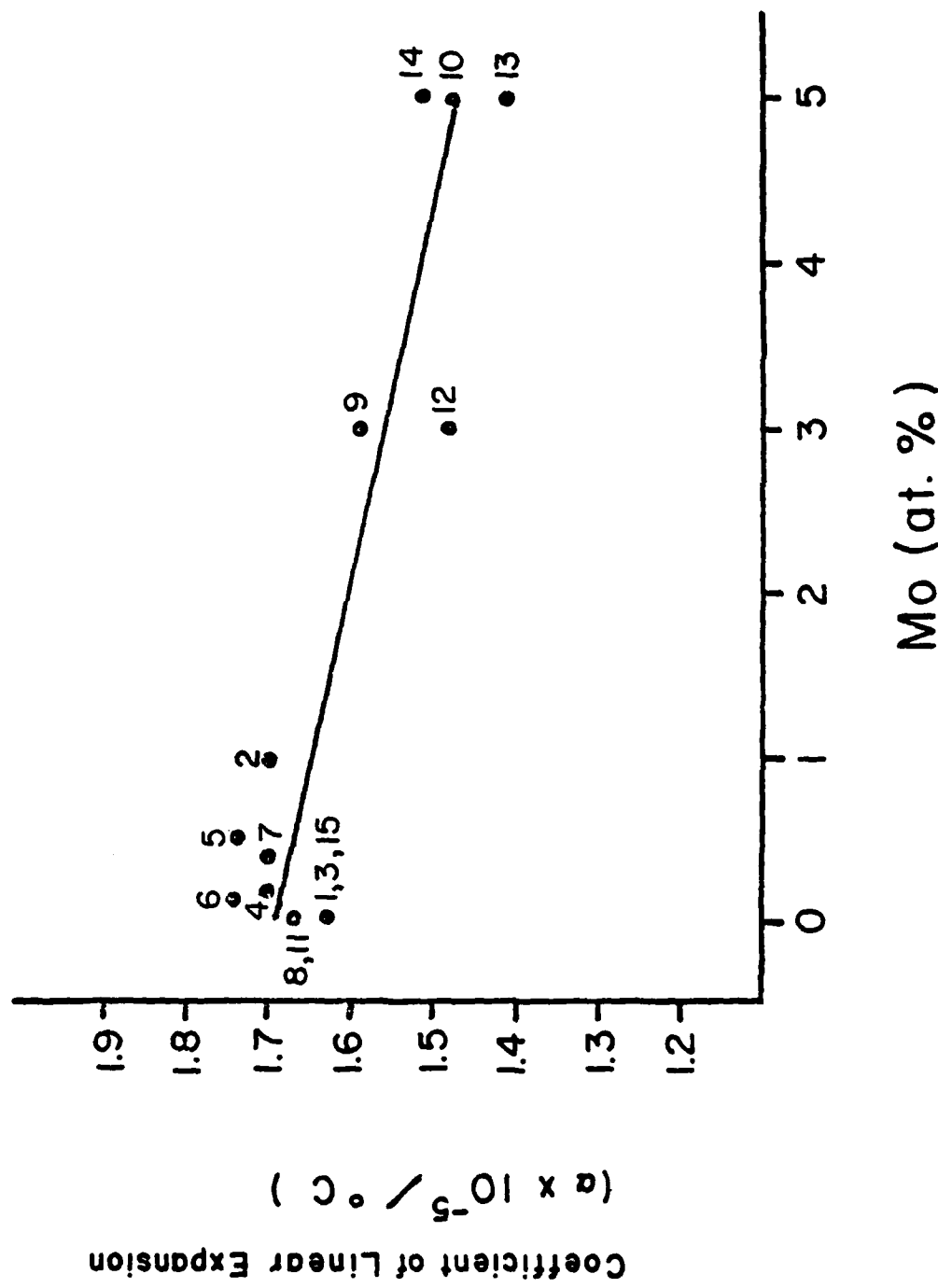
Figure 21 - Residual dislocation loops and shear band in alloy 10 tested at 800°C.

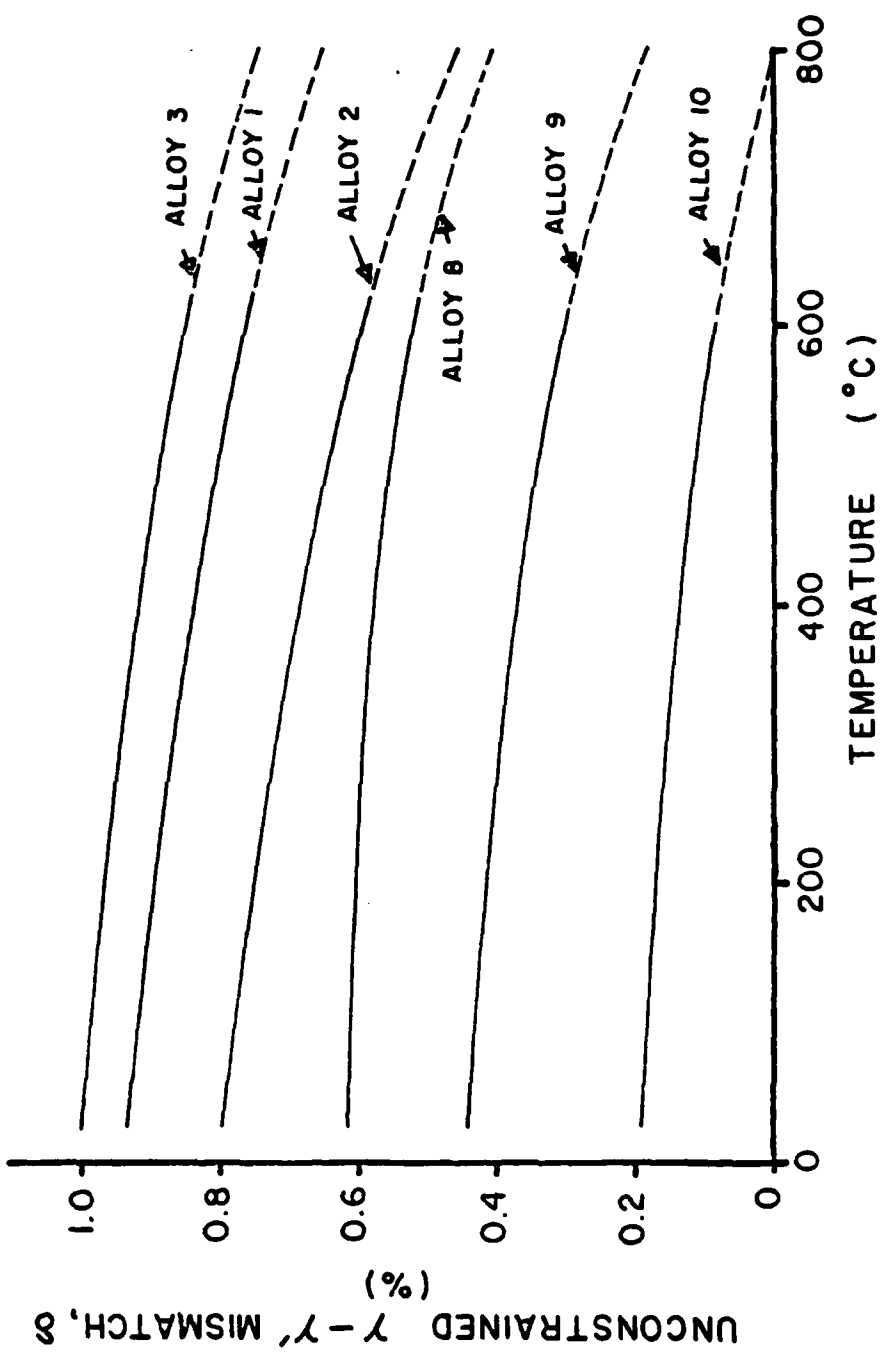
Figure 22 - Planar slip bands formed by 2% tensile strain in alloy 1 at 200°C. Peak-aged for 16.5 hours at 760°C.

Figure 23 - Deformation behavior of alloy 1 tested at 800°C.
a) Bright-field image of dislocation loops.
b) Dark-field image ($\bar{g} = 200$), (Z.A. = 001).

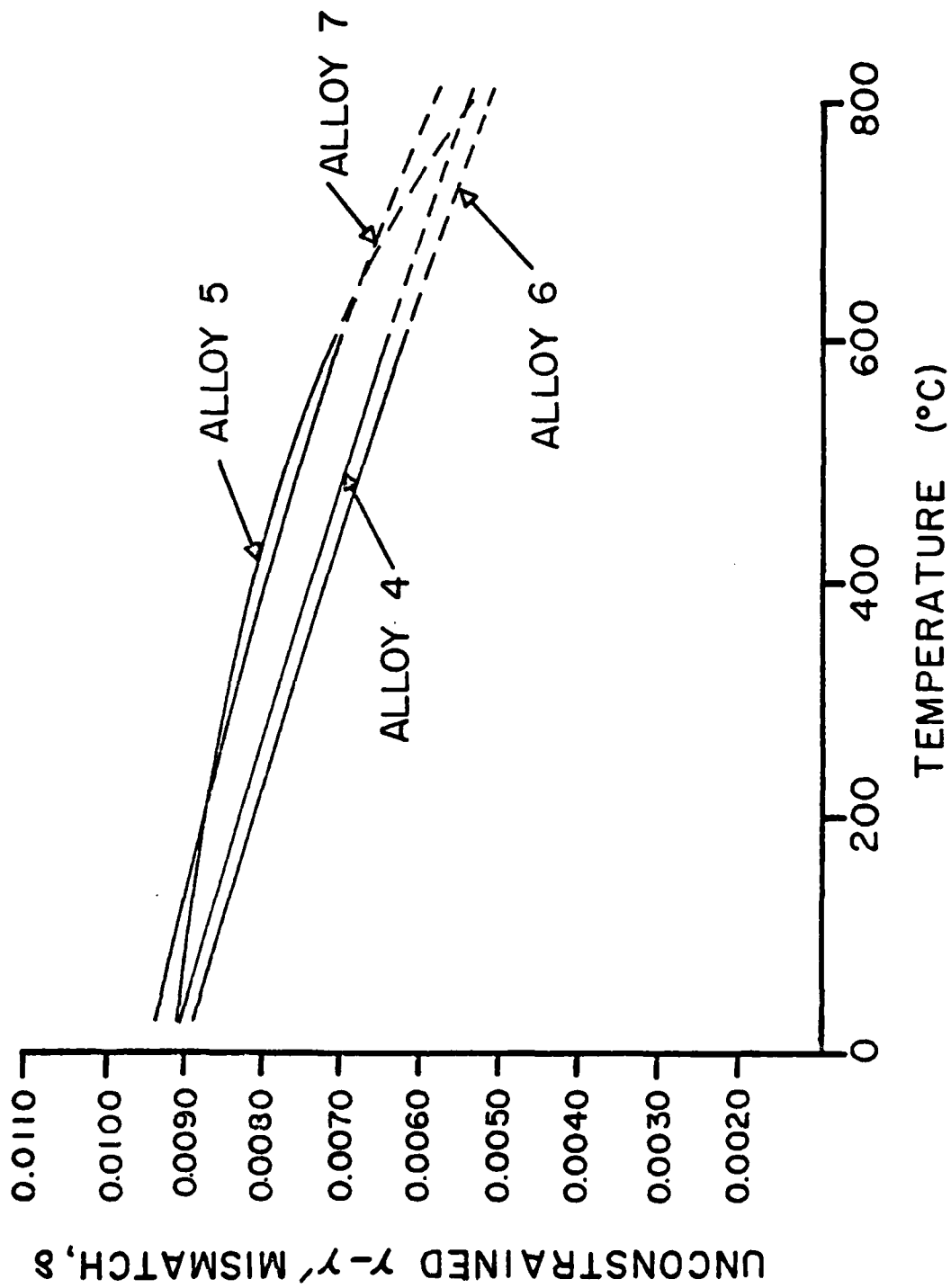
Figure 24 - Summary of the yielding behavior observed for the experimental Ni-Cr-Al-Ti - Mo alloys.



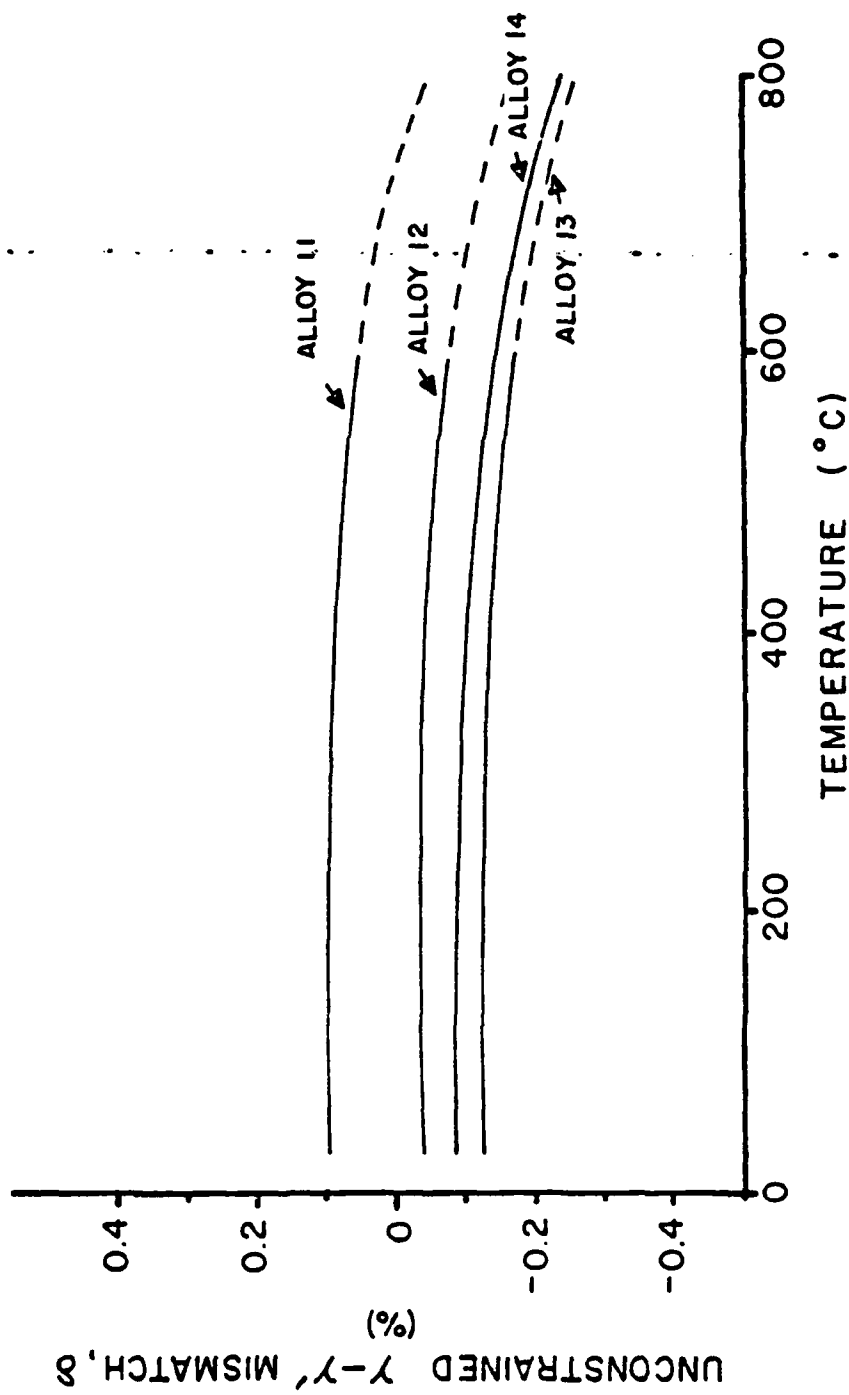


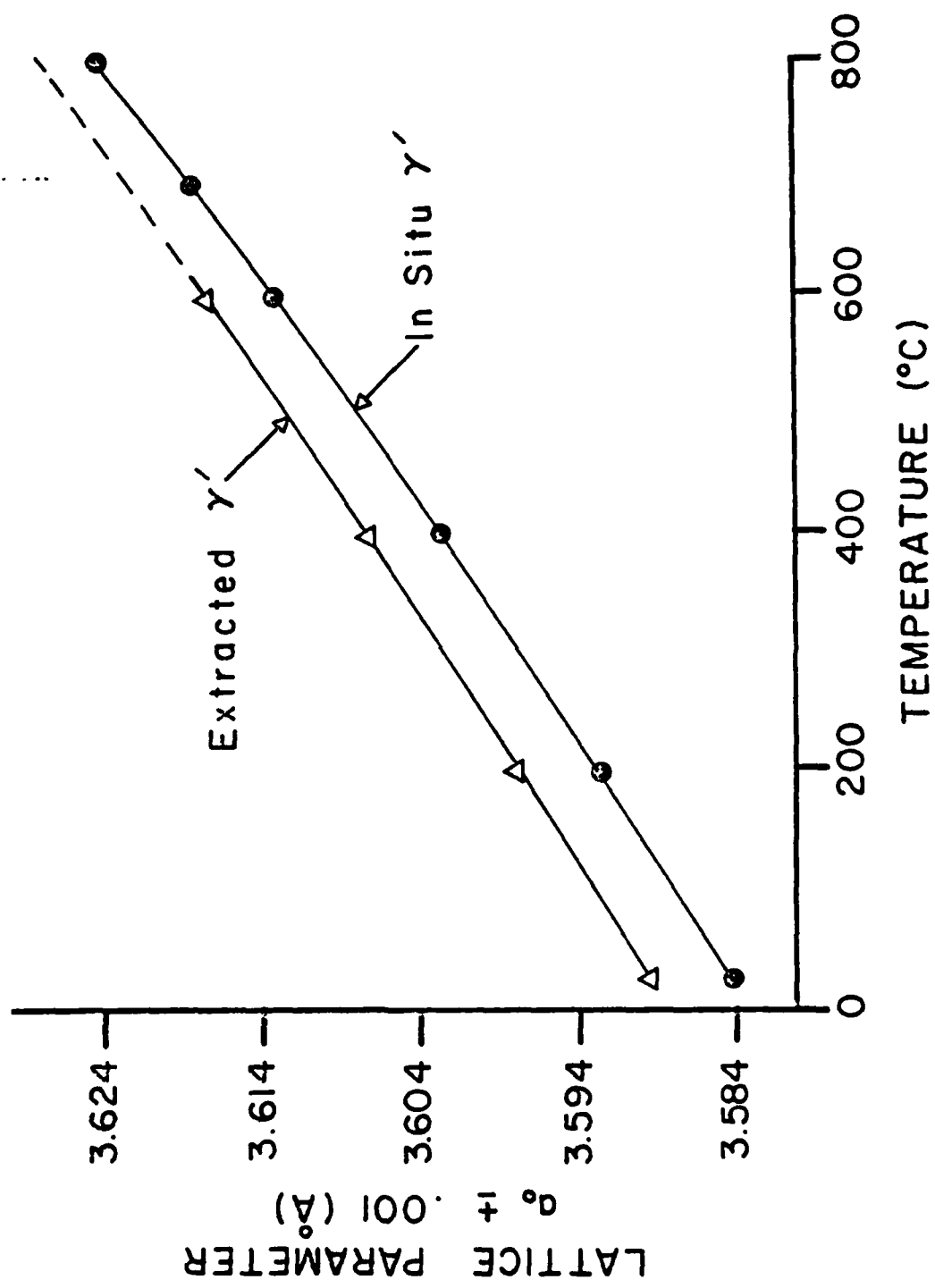


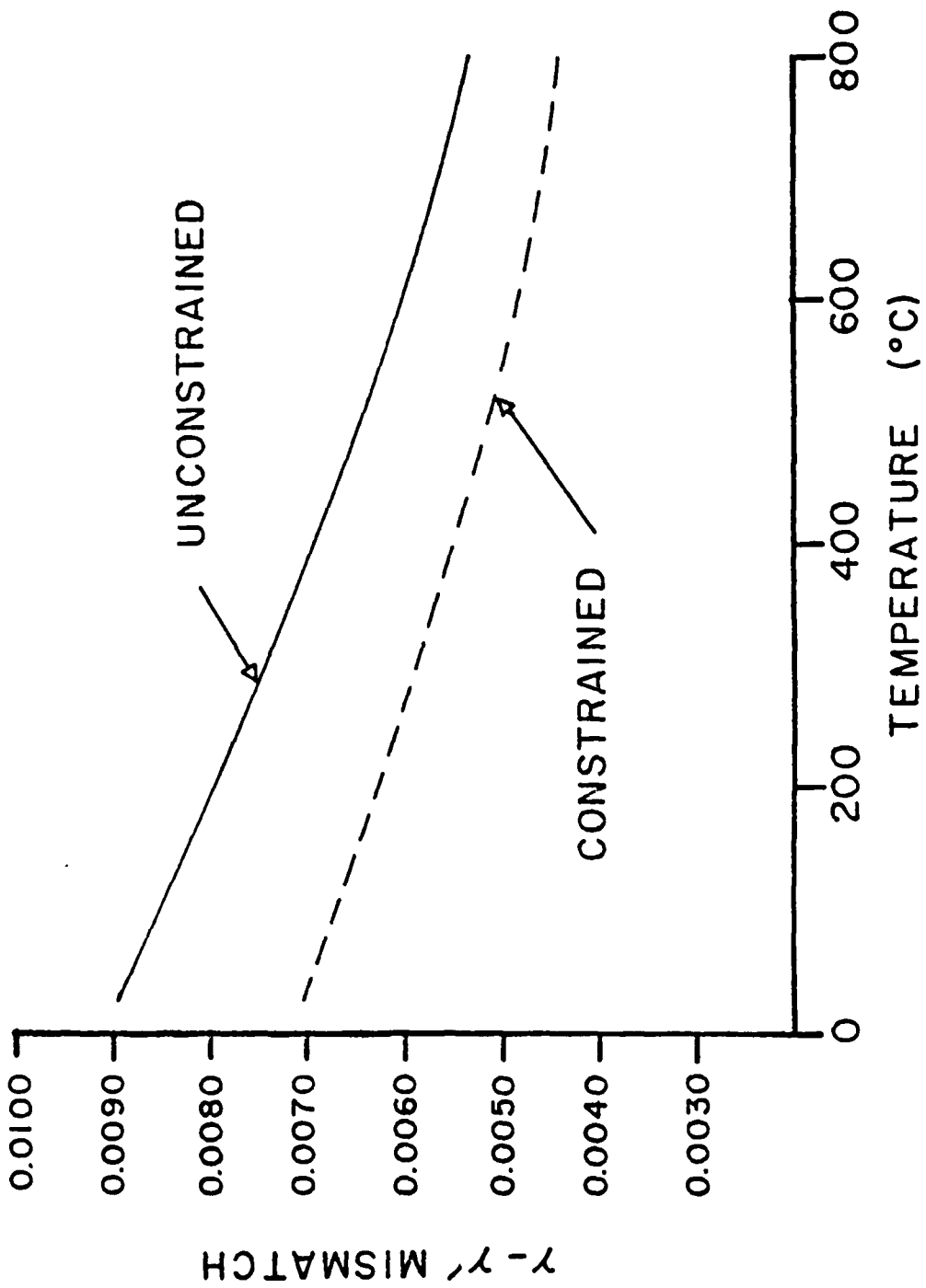
UNCONSTRAINED $\gamma - \gamma'$ MISMATCH, δ

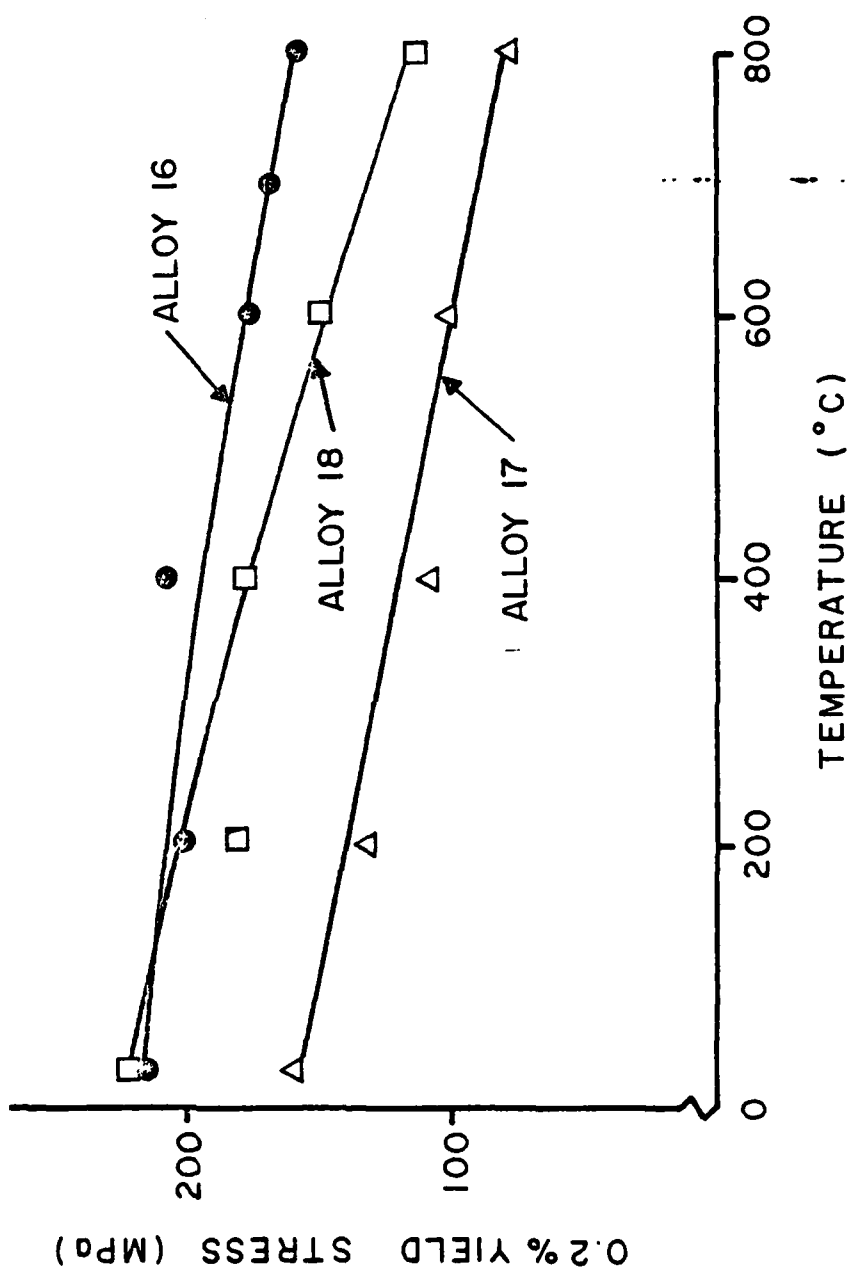


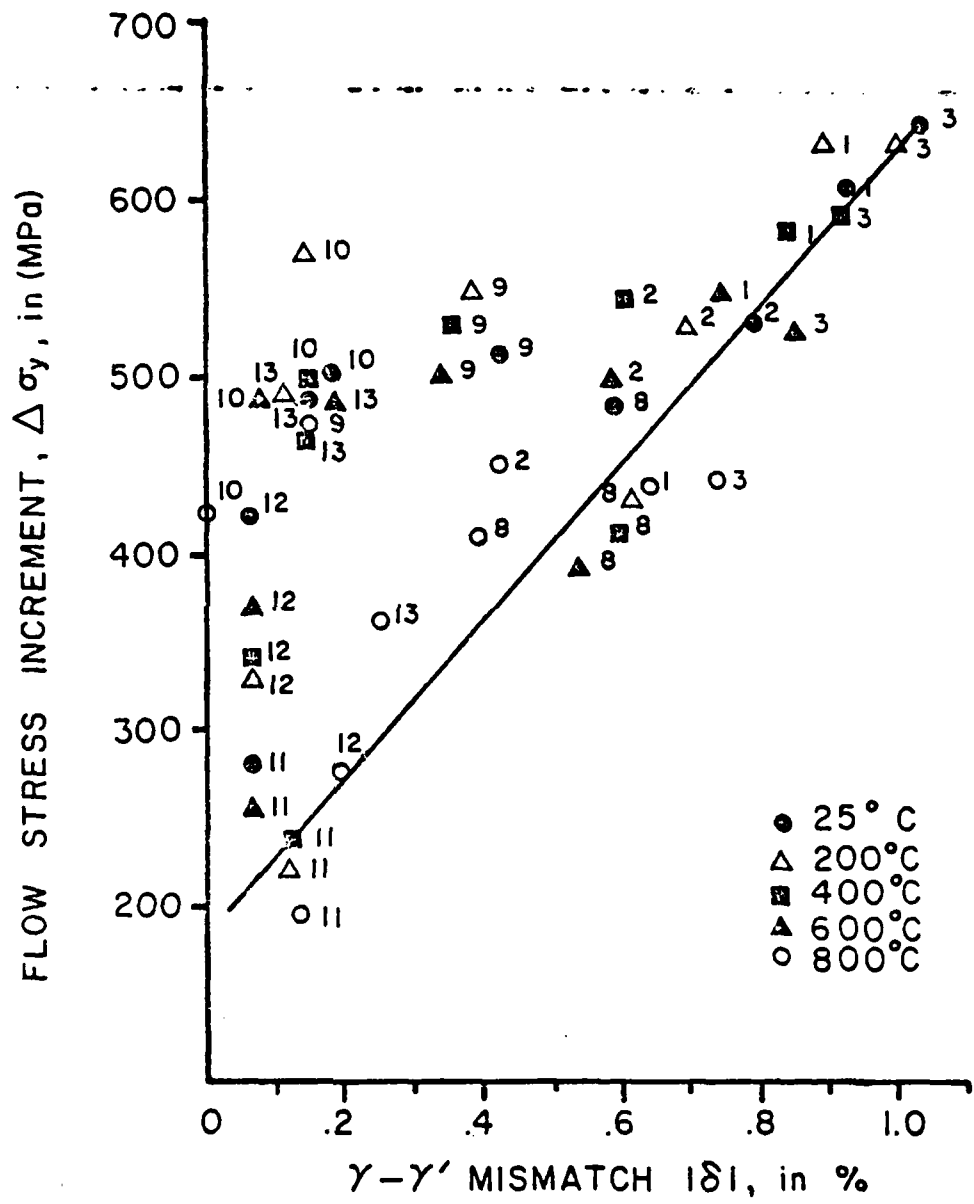
UNCONSTRAINED γ - γ' MISMATCH, δ

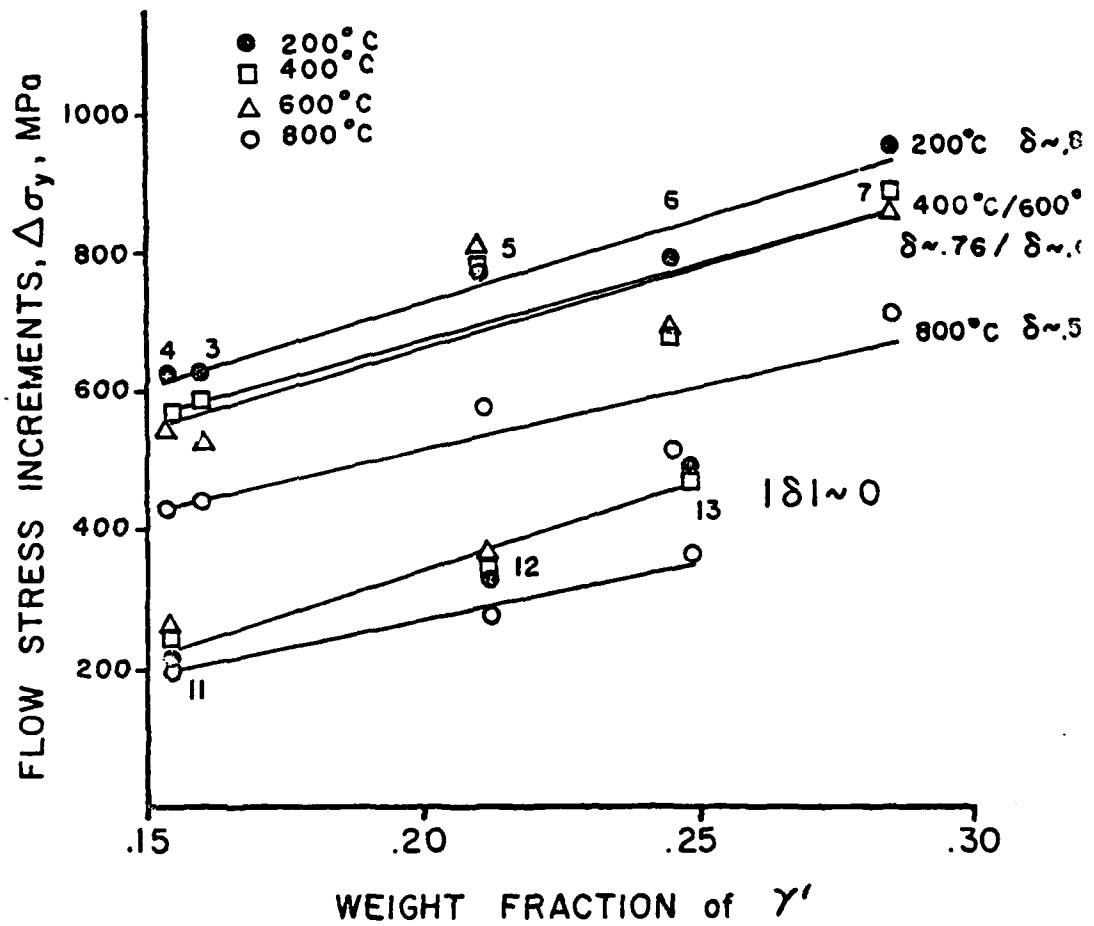


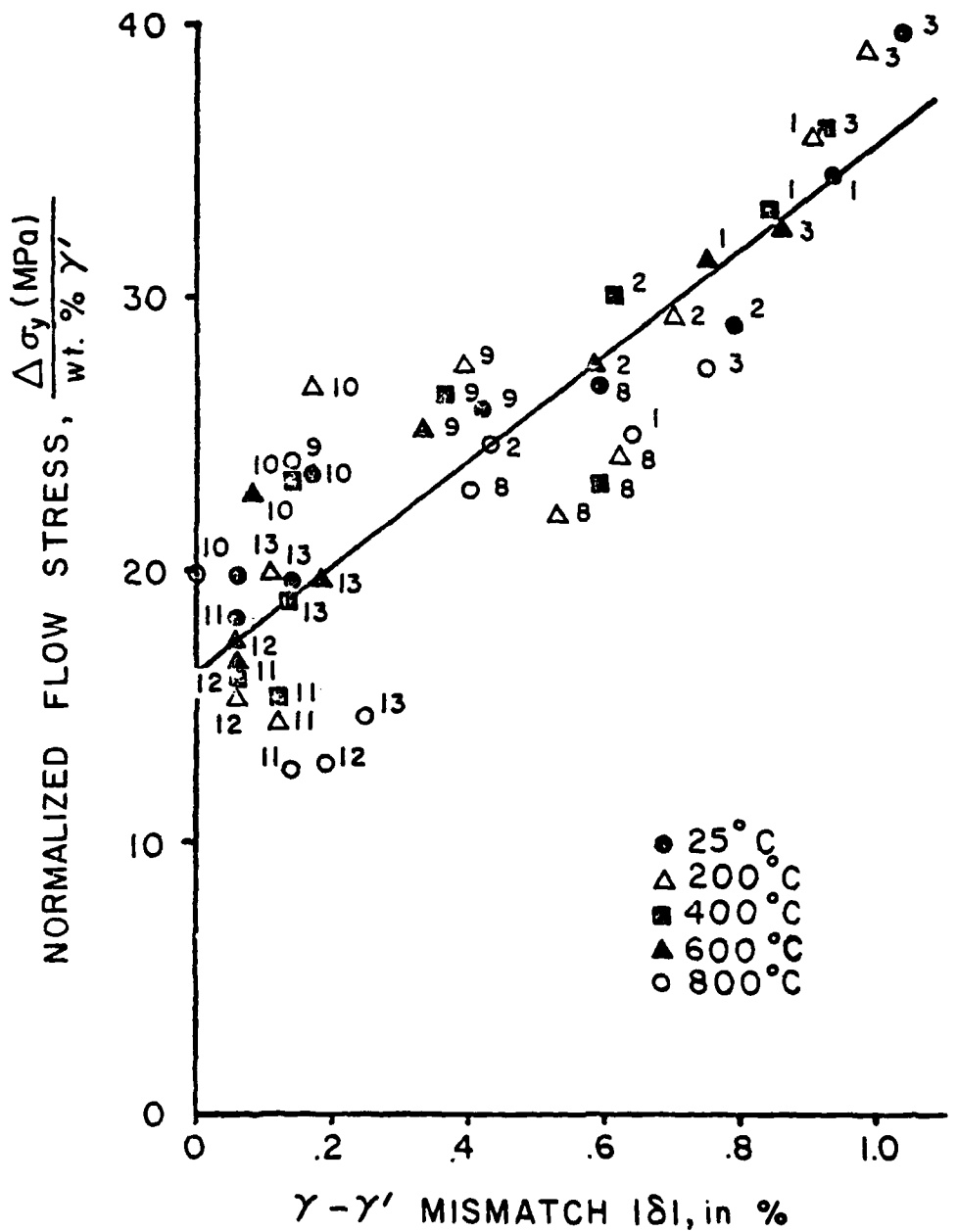


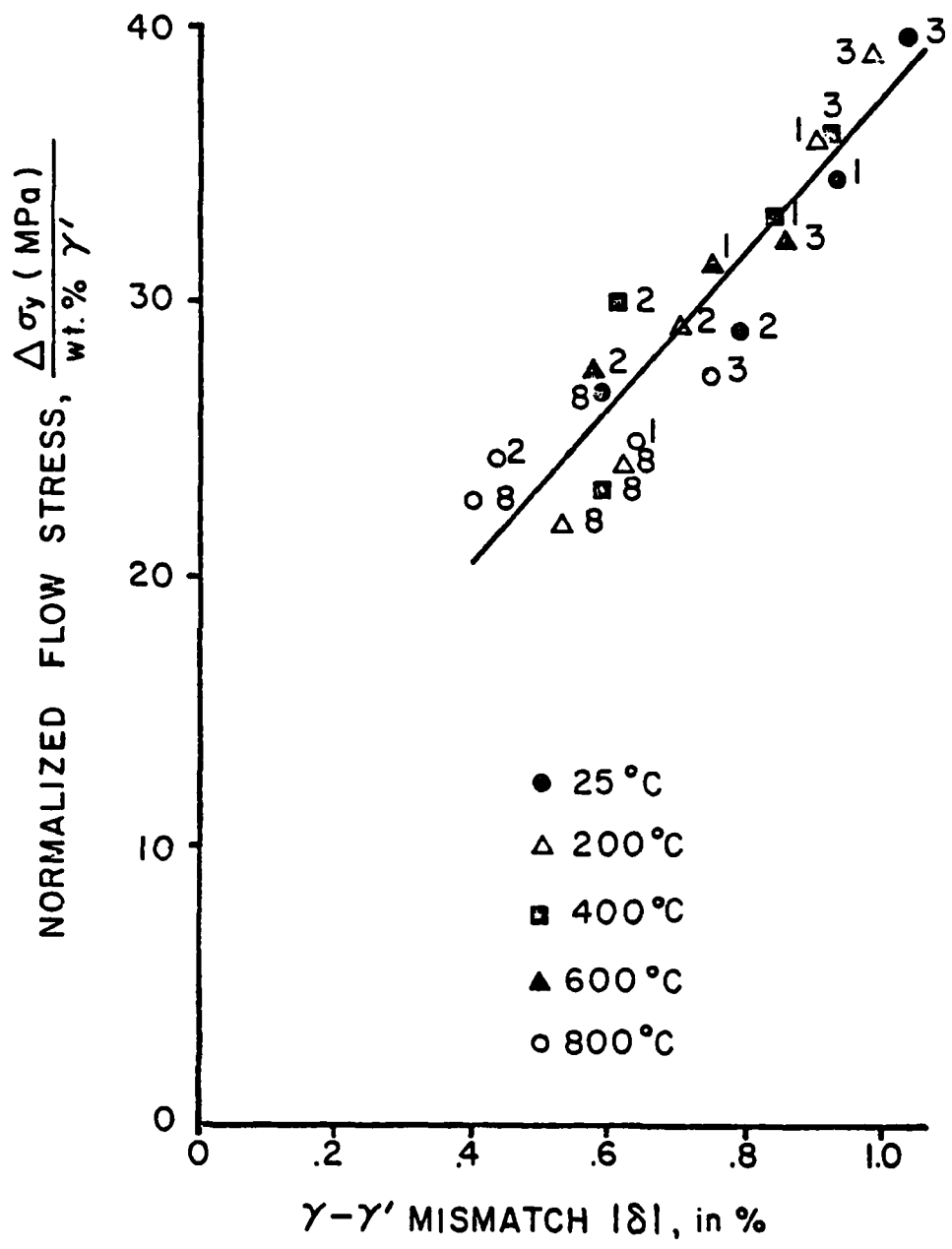


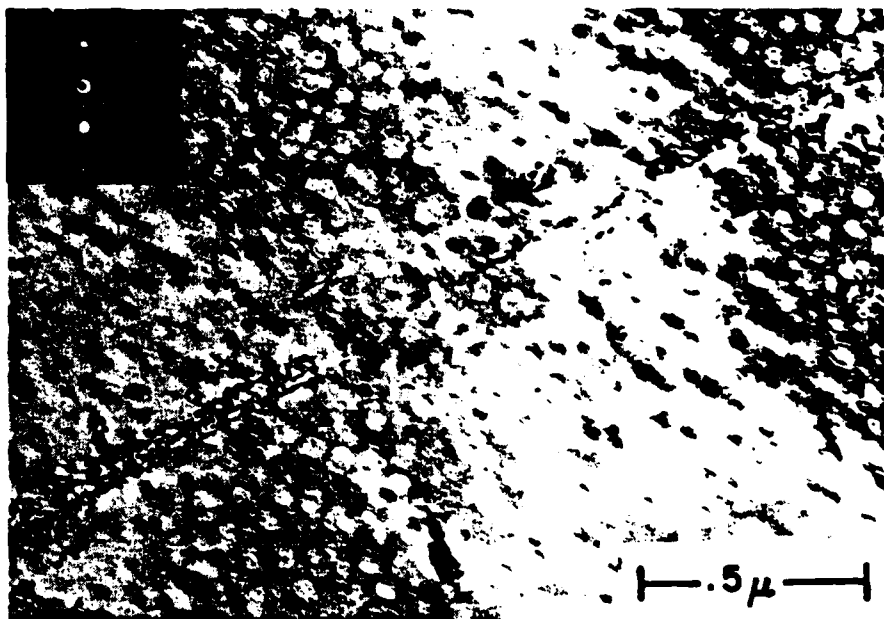




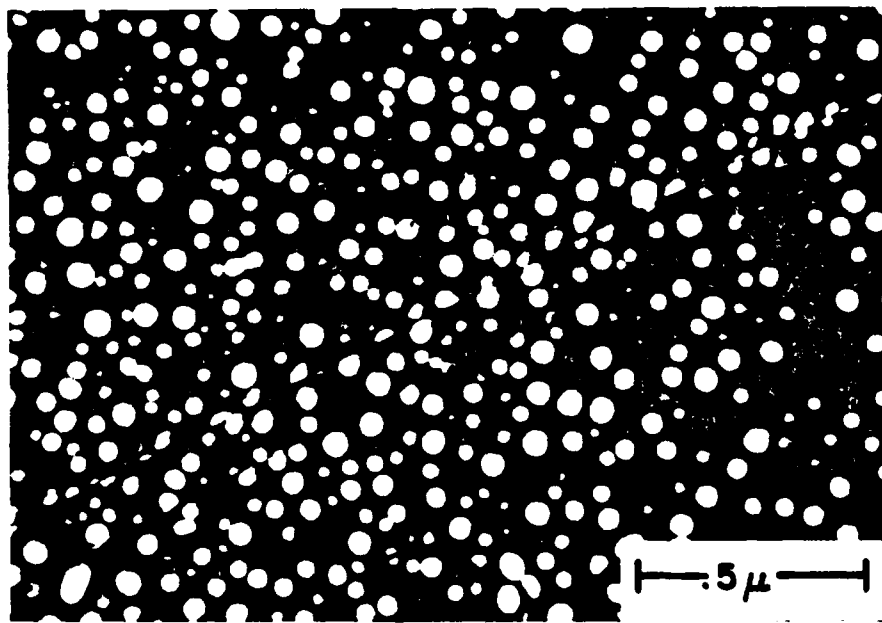






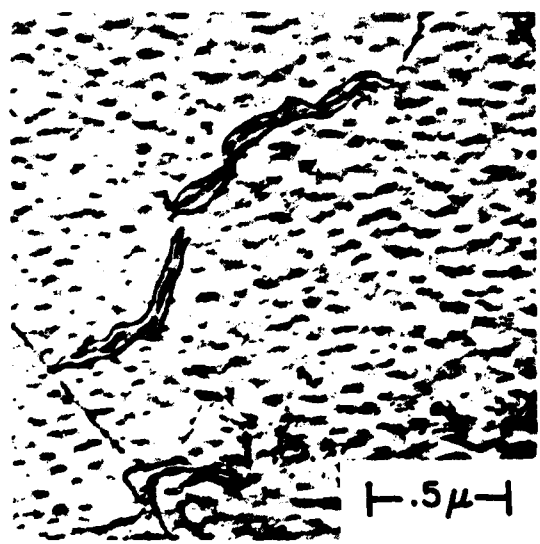


a

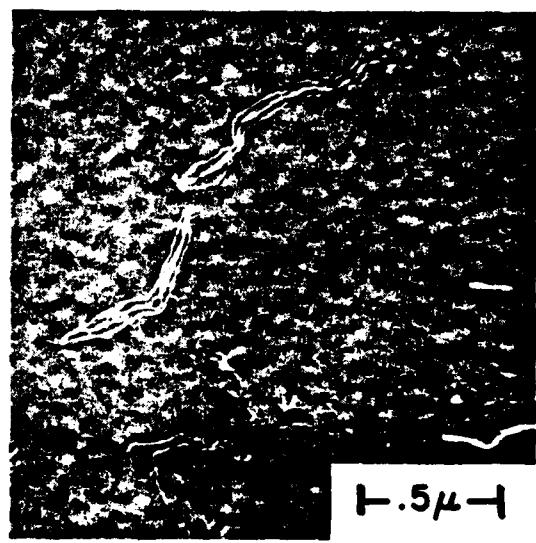


b





a



b

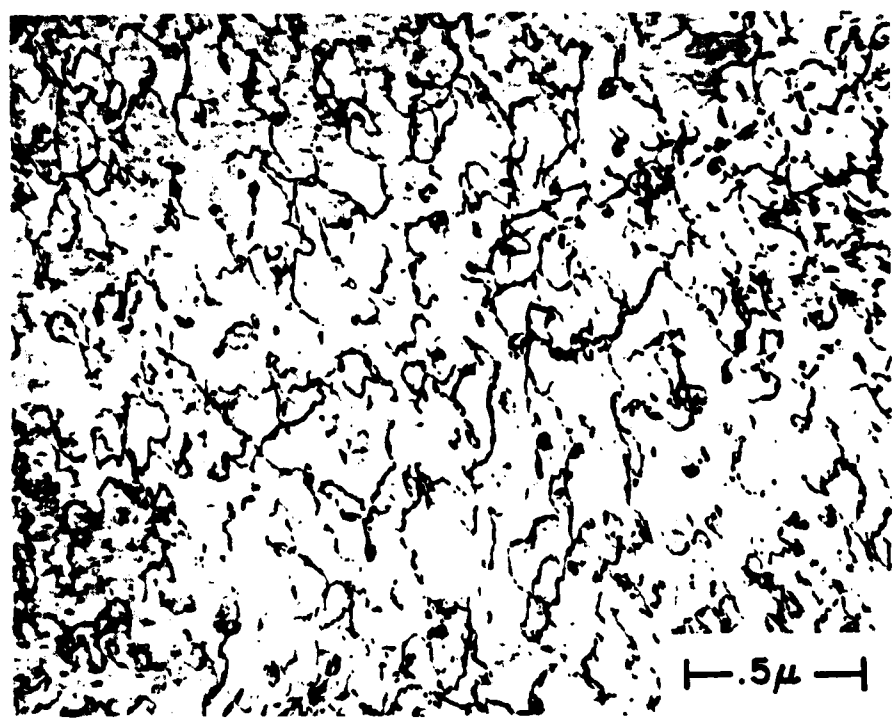


a

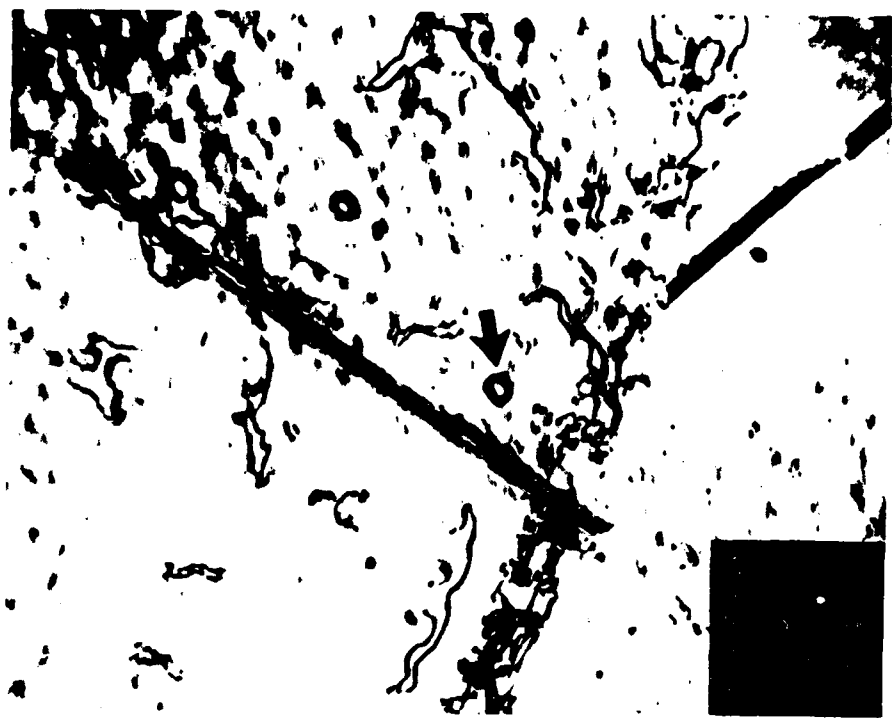
— 1 μ —



b



1μ

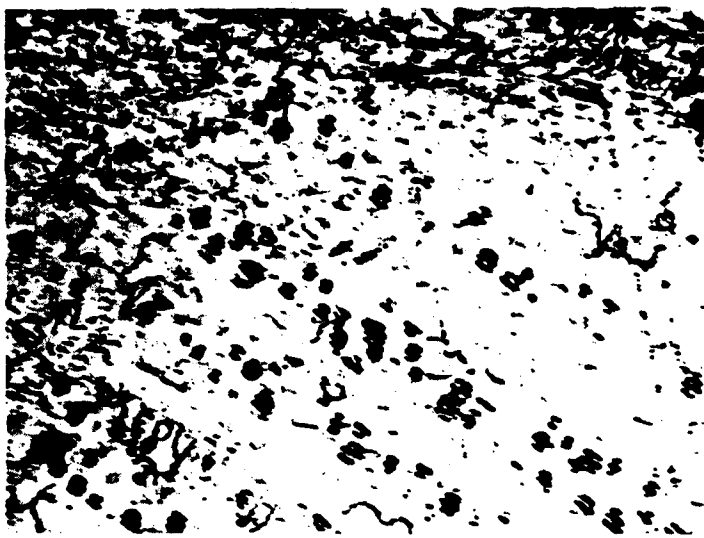




D

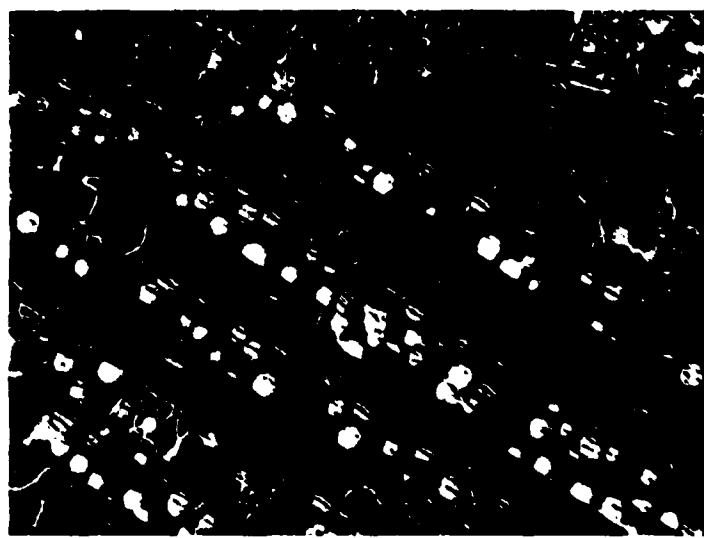


b

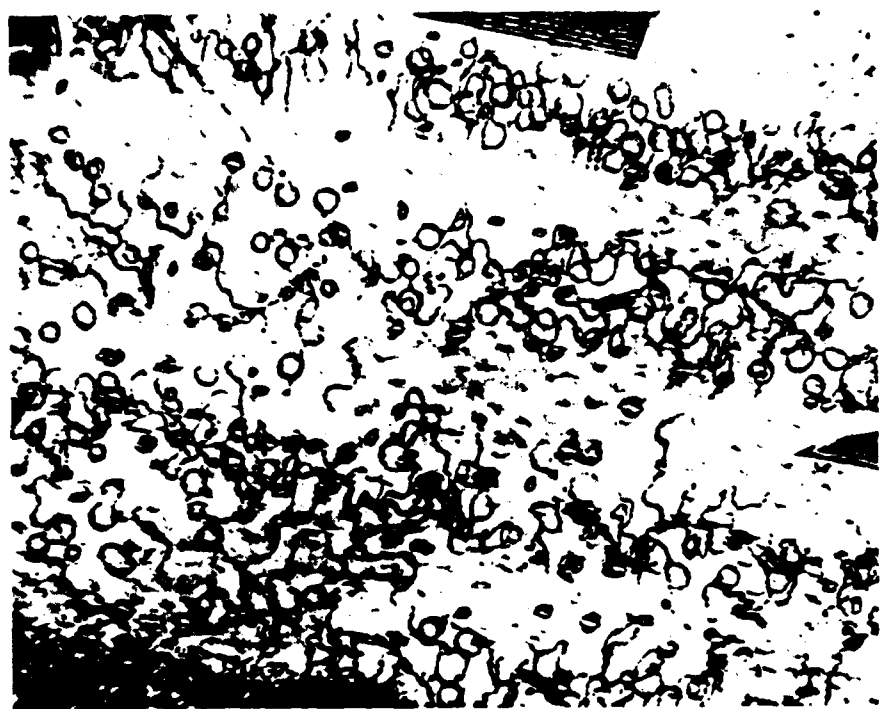


D

— 1 μ —



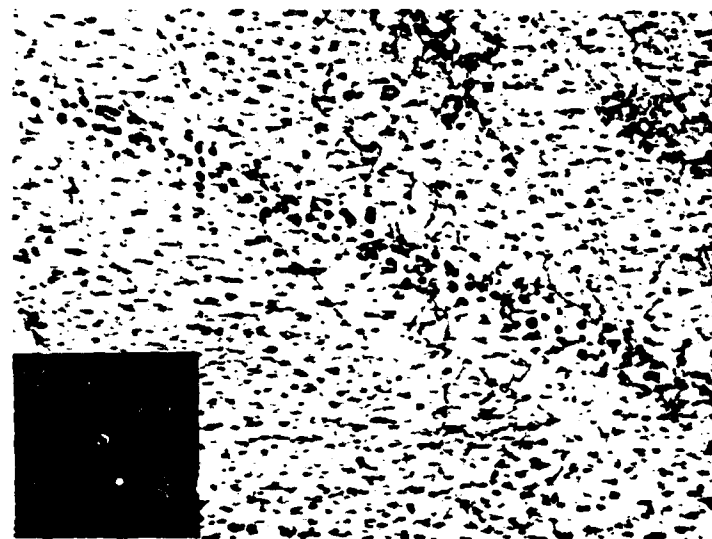
b



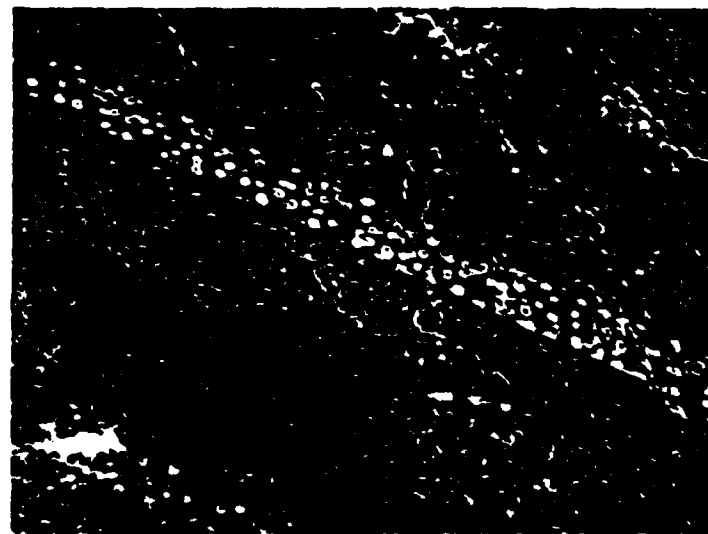
— 1 μ —



— 1 μ —

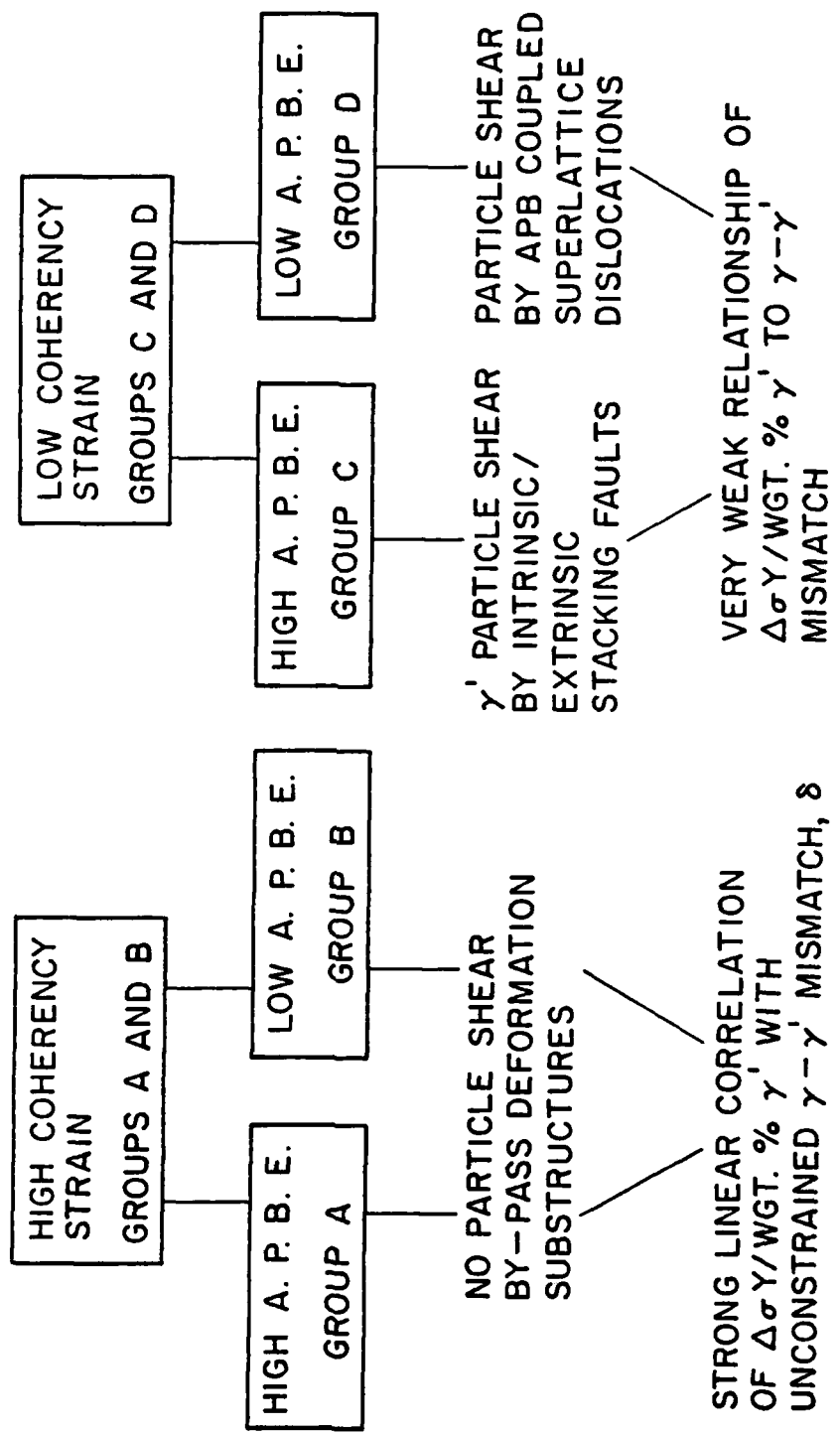


— 1 μ —



b

SUMMARY OF YIELDING BEHAVIOR



UNCLASSIFIED

SECURITY CLASSIFICATION OF THIS PAGE (When Data Entered)

REPORT DOCUMENTATION PAGE		READ INSTRUCTIONS BEFORE COMPLETING FORM
1. REPORT NUMBER TECHNICAL REPORT NO. 11	2. GOVT. ACCESSION NO. <i>AD A092 781</i>	3. RECIPIENT'S CATALOG NUMBER -----
4. TITLE (and Subtitle) THE INFLUENCE OF COHERENCY STRAIN ON THE ELEVATED TEMPERATURE TENSILE BEHAVIOR OF Ni-15Cr-Al-Ti-Mo ALLOYS	5. TYPE OF REPORT & PERIOD COVERED Technical Report	
7. AUTHOR(s) D. A. Grose and G. S. Ansell	6. PERFORMING ORG. REPORT NUMBER -----	
9. PERFORMING ORGANIZATION NAME AND ADDRESS Rensselaer Polytechnic Institute Troy, New York 12181	10. PROGRAM ELEMENT, PROJECT, TASK AREA & WORK UNIT NUMBERS -----	
11. CONTROLLING OFFICE NAME AND ADDRESS	12. REPORT DATE December 1980	
14. MONITORING AGENCY NAME & ADDRESS (if different from Controlling Office) METALLURGY PROGRAM, OFFICE OF NAVAL RESEARCH Department of the Navy 800 N. Quincy St., Arlington, Va. 22217	13. NUMBER OF PAGES 69	
16. DISTRIBUTION STATEMENT (of this Report) UNLIMITED	15. SECURITY CLASS. (of this report) Unclassified	
17. DISTRIBUTION STATEMENT (of the abstract entered in Block 20, if different from Report) -----	15a. DECLASSIFICATION/DOWNGRADING SCHEDULE -----	
18. SUPPLEMENTARY NOTES -----		
19. KEY WORDS (Continue on reverse side if necessary and identify by block number) Nickel-base alloys- precipitation hardening, coherency strains, creep, hot tensile, strengthening mechanisms		
20. ABSTRACT (Continue on reverse side if necessary and identify by block number) The effect of coherency strain on elevated temperature tensile strength was examined in a model, two-phase γ' -strengthened Ni-15Cr-Al-Ti-Mo alloy series. The temperature dependence of coherency strain as represented by the γ - γ' mismatch was determined over the temperature range 25°C to 300°C. The flow stress increment $\Delta\sigma_y$, due to precipitation of γ' , was found to correlate well to the magnitude of the γ - γ' mismatch over the same temperature interval. The correlation was strongest for high misfit alloys		

UNCLASSIFIED

SECURITY CLASSIFICATION OF THIS PAGE (When Data Entered)

regardless of the Antiphase Boundary Energy (APBE). The predominance of by-pass type dislocation-particle interactions in high coherency alloys confirms that strengthening is primarily due to coherency strains. Conversely, alloys with low misfit exhibit two distinct particle shear mechanisms believed to be dependent upon the relative APBE and matrix stacking fault energy of the alloy.

UNCLASSIFIED

SECURITY CLASSIFICATION OF THIS PAGE(When Data Entered)